

1 **Centroid moment tensor inversions of offshore earthquakes using a three-**
2 **dimensional velocity structure model: Slip distributions on the plate**
3 **boundary along the Nankai Trough**

4
5 **Authors**

6 **Shunsuke TAKEMURA^{1*}, Ryo OKUWAKI², Tatsuya KUBOTA³, Katsuhiko SHIOMI³**
7 **Takeshi KIMURA³, Akemi NODA⁴**

8 ¹**Earthquake Research Institute, the University of Tokyo, 1-1-1 Yayoi, Bunkyo-ku,**
9 **Tokyo, 113-0032, Japan**

10 ²**Mountain Science Center, Faculty of Life and Environmental Sciences, University**
11 **of Tsukuba, 1-1-1 Tennodai, Tsukuba 305-8572, Japan.**

12 ³**Network Center for Earthquake, Tsunami and Volcano, National Research Institute**
13 **for Earth Science and Disaster Resilience, 3-1 Tennodai, Tsukuba, Ibaraki, 305-0006,**
14 **Japan.**

15 ⁴**Earthquake and Tsunami Research Division, National Research Institute for Earth**
16 **Science and Disaster Resilience, 3-1 Tennodai, Tsukuba, Ibaraki, 305-0006, Japan.**

17
18
19
20 **Running Title**

21 3D CMT inversion along the Nankai Trough

22
23 **Corresponding Author**

24 Shunsuke Takemura

25 E-mail: shunsuke@eri.u-tokyo.ac.jp

26 Phone: +81 3-5841-5689

27

28 **Summary**

29 Due to complex three-dimensional (3D) heterogeneous structures, conventional one-
30 dimensional (1D) analysis techniques using onshore seismograms can yield incorrect
31 estimation of earthquake source parameters, especially dip angles and centroid depths of
32 offshore earthquakes. Combining long-term onshore seismic observations and numerical
33 simulations of seismic wave propagation in a 3D model, we conducted centroid moment
34 tensor (CMT) inversions of earthquakes along the Nankai Trough between April 2004 and
35 August 2019 to evaluate decade-scale seismicity. Green's functions for CMT inversions of
36 earthquakes with moment magnitudes of 4.3–6.5 were evaluated using finite-difference
37 method simulations of seismic wave propagation in the regional 3D velocity structure model.
38 Significant differences of focal mechanisms and centroid depths between previous 1D and
39 our 3D catalogues were found in the solutions of offshore earthquakes. By introducing the 3D
40 structures of the low-velocity accretionary prism and the Philippine Sea Plate, dip angles and
41 centroid depths for offshore earthquakes were well-constrained. Teleseismic CMT also
42 provides robust solutions but our regional 3D CMT could provide better constraints of dip
43 angles. Our 3D CMT catalogue and published slow earthquake catalogues depicted spatial
44 distributions of slip behaviours on the plate boundary along the Nankai Trough. The regular
45 and slow interplate earthquakes were separately distributed, with these distributions reflecting
46 the heterogeneous distribution of effective strengths along the Nankai Trough plate boundary.
47 By comparing the spatial distribution of seismic slip on the plate boundary with the slip-
48 deficit rate distribution, regions with strong coupling were clearly identified.

49

50 **Keywords:**

51 Computational seismology, earthquake ground motions, earthquake source observations,
52 seismicity and tectonics, wave propagation

53

54 **1. Introduction**

55 Focal mechanisms of earthquakes and their spatial distributions are important for
56 evaluating tectonic/local stress and strain fields (e.g. Saito *et al.* 2018, Terakawa & Matsu'ura
57 2010, Townend & Zoback 2006). To determine focal mechanisms, first-*P* or *S* polarisation
58 inversion (e.g. Hardebeck & Shearer 2002, Shelly *et al.* 2016) and waveform-based centroid
59 moment tensor (CMT) inversion (e.g. Dziewonski *et al.* 1981, Ekström *et al.* 2012, Kanamori
60 & Rivera 2008) techniques have been widely used around the world. One-dimensional (1D)
61 Earth models are assumed in typical focal mechanism determination methods. In regions with
62 complex three-dimensional (3D) heterogeneous structures, first-motion solutions using the
63 1D Earth model systematically show mis-estimations (e.g. Takemura *et al.* 2016). Although
64 CMT methods based on long-period (> 10 s) waveforms can be applied only for moderate-to-
65 large earthquakes due to signal-to-noise problems for long-period components, their
66 evaluations of source parameters are generally robust against structural heterogeneities in
67 comparison to first-motion solutions.

68 Along the Nankai Trough, megathrust earthquakes have repeatedly occurred at intervals of
69 100–150 years (e.g. Ando 1975). Evaluating seismicity around this region is important for
70 contributing to the understanding of megathrust earthquakes, such as evaluating stress
71 accumulation/release processes on plate boundaries. In Japan, regular and slow earthquakes
72 have been systematically monitored by the seismic networks of the Monitoring of Waves on
73 Land and Seafloor (MOWLAS; <https://doi.org/10.17598/NIED.0009>) operated by the
74 National Research Institute for Earth Science and Disaster Resilience (NIED; Okada *et al.*
75 2004). According to the combined earthquake catalogues of the International Seismological
76 Centre-Global Earthquake Model (ISC-GEM; Storchak *et al.* 2013), the Japan Meteorological
77 Agency (JMA), and the NIED F-net (Fukuyama *et al.* 1998, Kubo *et al.* 2002), the seismicity
78 of regular earthquakes along the Nankai Trough, especially interplate earthquakes, is quite
79 low. Figure 1 shows the spatial distribution of regular earthquakes with moment magnitudes
80 (M_w) of 4.3–6.5 that occurred from April 2004 to August 2019, as listed in the F-net moment
81 tensor (F-net MT) catalogue. The regional moment tensor inversion can be applied to
82 earthquakes with $M_w >$ about 4, which is smaller than a lower limit of teleseismic moment
83 tensor inversion (e.g., Figure 5 of Ekström *et al.* 2012). This is an advantage for discussing
84 detail seismicity in a certain region. A few shallow offshore earthquakes occurred in the
85 Tonankai and Nankai regions and their focal mechanisms in the F-net catalogue were not
86 characterised by low-angle thrust faulting. In other words, no earthquakes suggesting faulting

87 on the plate boundary around the Tonankai and Nankai regions are listed in the F-net MT
88 catalogue.

89 On 1 April 2016, the M_w 5.8 earthquake, called “2016 southeast off the Kii Peninsula
90 earthquake”, occurred in the Tonankai region (marked A in Figure 1). The F-net MT solution
91 of this earthquake was characterised by high-angle (38°) reverse faulting below the upper
92 surface of the Philippine Sea Plate, indicating it was an intraslab earthquake. However, a
93 detailed analysis of this earthquake revealed that it could be modelled by low-angle thrust
94 faulting at a depth of approximately 10 km, suggesting seismic slip along the plate boundary
95 (e.g. Nakano *et al.* 2018a, Takemura *et al.* 2018a, Wallace *et al.* 2016). Source models
96 suggested in these studies were also consistent with a model based on observed tsunami data
97 (Kubota *et al.* 2018). In regions with a thick accretionary prism, characteristics of surface
98 wave propagation are significantly affected by a low-velocity accretionary prism (e.g.
99 Gomberg 2018, Kaneko *et al.* 2019, Shapiro *et al.* 1998). Thus, the focal mechanisms of other
100 offshore earthquakes along the Nankai Trough could be incorrectly estimated using
101 conventional 1D regional MT inversion, even for long-period displacements. Indeed, shallow
102 very low frequency earthquakes along the Nankai Trough have been interpreted as low-angle
103 thrust faulting on the plate boundary by using offshore seismic observations (e.g. Nakano *et*
104 *al.* 2018b), but their focal mechanisms based on 1D analysis of onshore observations were
105 high-angle reverse faulting mechanisms within the accretionary prism (e.g., Ito & Obara
106 2006). To evaluate seismic activity along the Nankai Trough more precisely, offshore
107 earthquakes listed in the previous 1D catalogues require re-analysis.

108 Parallel simulation codes of seismic wave propagation (e.g. Gokhberg & Fichtner 2016,
109 Maeda *et al.* 2017) and 3D seismic velocity structure models (e.g. Eberhart-Phillips *et al.*
110 2010, Koketsu *et al.* 2012) enable the simulation of Green’s functions propagating through
111 realistic 3D Earth models (hereafter called ‘3D Green’s functions’), which have been used to
112 develop CMT inversions (e.g. Hejrani *et al.* 2017, Lee *et al.* 2013, Okamoto *et al.* 2018,
113 Ramos-Martínez & McMechan 2001, Takemura, *et al.* 2018ab, 2019, Wang & Zhan 2020).
114 Although the resolution of detailed source characteristics for offshore earthquakes derived
115 using the 3D CMT method and onshore seismograms is limited compared to those using
116 offshore observations, these methods provide similar focal mechanisms and centroid
117 locations (see Figure 2 of Takemura *et al.* 2018b). Thus, offshore seismic activity, including
118 earthquakes before offshore seismic observations, can be effectively evaluated.

119 To investigate the decade-scale seismicity of offshore earthquakes along the Nankai

120 Trough, we re-evaluated focal mechanisms based on CMT inversion using 3D Green's
121 function datasets, which were evaluated by numerical simulations of seismic wave
122 propagation in a regional 3D velocity structure model. Then, to investigate spatial variation in
123 slip behaviours on the plate boundary along the Nankai Trough, we compared the spatial
124 distribution of focal mechanisms based on the 3D CMT technique with the spatial
125 distribution of slip-deficit rates (Noda *et al.* 2018), slow slip events (SSEs; Kobayashi 2014,
126 Miyazaki *et al.* 2006, Nishimura *et al.* 2013, Takagi *et al.* 2016, 2019, Yokota & Ishikawa
127 2020), shallow low-frequency tremors (LFTs; Yamashita *et al.* 2015), shallow very low-
128 frequency earthquakes (VLFs; Takemura *et al.* 2019b), and the 1968 Hyuga-nada
129 earthquake (Yagi *et al.* 1998).

130

131 **2. Data and Methods**

132 We used three-component (NS, EW, and UD) velocity seismograms from F-net (NIED
133 2019), for which the performance of the sensors have been systematically monitored (Kimura
134 *et al.* 2015). To conduct CMT inversion of the target earthquakes, we applied a band-pass
135 filter with passed periods of 25–100 s. We selected a 25–100 s period band because ground
136 motions for periods of 8–20 s are significantly affected by internal structures of the
137 accretionary prism along the Nankai Trough (e.g. Takemura *et al.* 2019a). The selected period
138 band is enough longer than corner periods of source spectra for target earthquakes. In our
139 CMT inversions, we used 10-min F-net velocity seismograms from three minutes before the
140 initial origin minute to conduct pre-processing (filter and integration) stably. We obtained
141 displacement waveforms by calculating time integration of each filtered velocity record. The
142 target earthquakes occurred within the region of assumed source grids (grey crosses in Figure
143 2) between April 2004 and August 2019, and values of M_w in the F-net catalogue ranging
144 from 4.3 to 6.5. According to the signal-to-noise ratios for the target period band, the
145 magnitude range of the analysed earthquake was determined by trial and error. Source grids
146 were uniformly distributed at horizontal intervals of 0.1° . Depths of source grids ranged from
147 6 to 50 km at an interval of 2 km. The total number of source grids was 61,433.

148 Green's functions were evaluated by solving equations of motion in the 3D viscoelastic
149 medium model based on the finite-difference method (FDM) simulations. The 3D simulation
150 model covered an area of $900 \times 1,000 \times 100 \text{ km}^3$, which was discretised by grid intervals of
151 0.5 km in the horizontal direction and 0.2 km in the vertical direction. We used a parallel
152 simulation code of OpenSWPC (Maeda *et al.* 2017), which includes the reciprocal calculation

153 mode for effectively evaluating Green's functions. The reciprocal calculation has proved very
154 useful in the case that the number of seismic source grids is significantly larger than the
155 number of seismic stations (e.g. Eisner & Clayton 2001, Hejrani *et al.* 2017, Okamoto *et al.*
156 2018). We obtained a total of approximately 35,000,000 Green's function SAC files from
157 61,433 source grids to 32 F-net stations (black and blue filled triangles in Figure 2) via 96
158 reciprocal FDM calculations. The source time function of each Green's function was the
159 K pper wavelet with a duration of 1 s.

160 The 3D velocity model of Koketsu *et al.* (2012) was used, as it has been widely applied in
161 studies of seismic ground motions across Japan. The configurations of the subducting oceanic
162 plate and the Moho discontinuity are consistent with other models (e.g., Hirose *et al.* 2008,
163 Shiomi *et al.* 2006). The oceanic crust of the model of Koketsu *et al.* (2012) has
164 approximately 7 km thickness, which correspond to those by seismic surveys (e.g., Nakanishi
165 *et al.* 2002). The topography model in our simulations was the ETOPO1 model (Amante &
166 Eakins 2009). The P - and S -wave velocities and density (V_P , V_S and ρ) in the seawater layer
167 were 1.5 km/s, 0.0 km/s and 1.04 g/cm³, respectively. The air column was modelled as a
168 vacuum with V_P of 0.0 km/s, V_S of 0.0 km/s and ρ of 0.001 g/cm³. The minimum V_S in the
169 solid column of 1.5 km/s was assumed. The accretionary prism is important for constraining
170 centroid depth but detail velocity structure within the accretionary prism has limited effects
171 on long-period (> 20 s) seismograms (Figures 5 and 6 of Takemura *et al.* 2019a).

172 Simulations were conducted using the computer system of the Earthquake and Volcano
173 Information Center at the Earthquake Research Institute, the University of Tokyo. Each
174 simulation required 385 GBytes of computer memory and a wall-clock time of 2.5 hours and
175 was performed using parallel computing with 432 cores to evaluate seismic wave propagation
176 of 200 s with 20,000 time-step calculations. According to our grid and model settings, our
177 FDM simulation can precisely evaluate long-period (> 10 s) seismic wave propagation.

178 Examples of Green's functions are illustrated in the right panels of Figure 2. The source
179 (red star) was located at a depth of 10 km, near the plate boundary. We employed the
180 Cartesian coordinate system of Aki & Richards (2002), where x , y , and z are taken as north,
181 east, and down, respectively. Due to the low-velocity accretionary prism and seawater,
182 durations of surface waves were amplified and elongated. In particular, for $M_{xy} = 1.0$ (i.e. a
183 pure strike-slip with strike angle of 0 $^\circ$, dip angle of 90 $^\circ$, and rake angle of 0 $^\circ$), Love waves on
184 horizontal components were strong and long. We assumed six-element moment tensors for
185 the CMT inversions, which includes five double couple and an isotropic moment tensors (e.g.

186 Kikuchi & Kanamori 1991).

187 In the CMT inversions, we basically used Green's functions at F-net stations within
188 epicentral distances of 100–400 km from the initial epicentre. The initial epicentre was
189 obtained from the F-net MT catalogue. In cases where earthquake $M_w < 4.5$, we selected a
190 distance range of 100–350 km due to the signal-to-noise ratio of the observed waveforms for
191 the analysed period. We visually checked the filtered displacement waveforms and discarded
192 noisy ones. Centroid location and time of the analysed earthquake were determined using grid
193 search inversion. Because the analysis period range was longer than the source durations of
194 target earthquakes with $M_w = 4.3–6.5$, we did not estimate source durations of these events. A
195 set of Green's functions at the source grids, which were located in a $\pm 0.4^\circ$ region from the
196 initial epicentre and were distributed at depths of 6–50 km, was selected for the grid search
197 inversion.

198 The CMT inversions were conducted for each selected source grid every 1 s from three
199 minutes before the origin minute as recorded in the F-net catalogue. We used a 200-s time
200 window for each CMT inversion. During grid search CMT inversion, we did not allow time
201 shifts between synthetic and observed seismograms. After CMT inversion at all of the
202 selected source grids, we obtained seismic moments and focal mechanisms at all locations
203 and times. To identify the optimal solution, we evaluated variance reductions (VRs) between
204 the observed and synthetic displacement seismograms for periods of 25–100 s. The VR
205 could then be evaluated using the following equation:

$$VR = \left[1 - \frac{\sum_{i=1}^{N_S} \int (u_i^{obs.}(t) - u_i^{syn.}(t))^2 dt}{\sum_{i=1}^{N_S} \int (u_i^{obs.}(t))^2 dt} \right] \times 100 [\%] \quad (1)$$

206 where N_S is the number of stations and $u_i^{obs.}$ and $u_i^{syn.}$ are the time-series of observed
207 and synthetic displacements, respectively. If observed and synthetic seismograms are
208 perfectly matched, VR is 100 %. The solution with the maximum VR was considered the
209 optimal solution, providing the optimal centroid location, depth, time, focal mechanism, and
210 seismic moment of each earthquake. In the case that the optimal solution was located at the
211 edges of the initial source grids, we performed the CMT inversion again using Green's
212 functions for a broader source grid dataset. In the cases of regions around the edges of all
213 source grids (all crosses in Figure 2), such as southern Kyushu and eastern Izu, we could not
214 extend the grid set and then the optimal solution was located at the grid edge. These events
215 may include possibilities of some shifts outside the edges of the assumed source grids. Our
216 grid search CMT inversion required approximately 15–20 minutes using a typical, single-core

217 desktop machine.

218

219 **3. Results**

220 We obtained a total of 215 CMT solutions for moderate earthquakes that occurred between
221 April 2004 and August 2019. We discarded the solutions with a maximum VR of less than
222 20%. Our 3D CMT catalogue is listed in Global CMT (GCMT) format in the Supplementary
223 data (Table S1) and the CSV format full catalogue data is available from
224 <https://doi.org/10.5281/zenodo.3674161>. The size distribution and magnitude-time diagram
225 of our 3D CMT catalogue are shown in Figures S1 and S2. The estimated moment
226 magnitudes were slightly changed from the original F-net catalogue. The VRs of earthquakes
227 with small magnitudes tended to be low (Figure S2) due to the signal-to-noise ratio for the
228 analysed period range. We also compared our results with the GCMT catalogue (Figure S1).
229 Teleseismic CMT inversion is robust but our regional CMT catalogue contains more
230 earthquakes, whose M_w values are less than about 5.

231 Figures 3 and 4 show examples of CMT solutions for the southeast off the Kii Peninsula
232 earthquake (1 April 2016) and the Hyuga-nada earthquake (9 May 2019), respectively. In our
233 previous study (Takemura *et al.* 2018a), the 2016 southeast off the Kii Peninsula earthquake
234 was also analysed. The epicentre location and origin time were fixed in the previous study.
235 We re-analysed this earthquake via full 3D CMT inversion, which estimates centroid
236 location, depth, time, and moment tensor. The F-net MT solution of this earthquake was a
237 high-angle (38°) reverse faulting mechanism (grey focal sphere in Figure 3). Its optimal
238 solution is a M_w 5.9 low-angle (10°) thrust faulting at a depth of 10 km (Figure 3), where the
239 plate boundary closely exists (e.g. Kamei *et al.*, 2012; Park *et al.*, 2010). The synthetic
240 seismograms of the optimal solution corresponded well with the observations. The depth
241 variation of VRs illustrated a clear peak around the optimal depth. The centroid depth of this
242 earthquake was well constrained by our CMT inversion. Takemura *et al.* (2018a) numerically
243 demonstrated that the low-velocity accretionary prism just above the seismic source—which
244 controls long-period surface wave propagation—provides a better constraint on the centroid
245 depth. They also demonstrated that the 3D oceanic plate has an important role for
246 constraining focal mechanism (Figures 7 and 8 of Takemura *et al.* 2018a).

247 The centroid location was also close to that estimated by ocean-bottom seismometers
248 deployed just above the source region (Nakano *et al.* 2018a, Wallace *et al.* 2016), while the
249 GCMT solution was slightly (0.2°) shifted to the south (Figure S3). The CMT result was

250 consistent with models estimated by offshore observations (Kubota *et al.* 2018, Nakano *et al.*
251 2018a, Wallace *et al.* 2016). Especially, by using travel times, tsunami, and afterslip records,
252 Wallace *et al.* (2016) and Nakano *et al.* (2018a) concluded that this earthquake can be
253 interpreted as an interplate earthquake. Our CMT solution based on 3D Green's functions and
254 onshore seismograms also suggests this earthquake was considered as faulting on the plate
255 boundary.

256 Figure 4 shows the results of the CMT inversion and waveform fitting for the Hyuga-nada
257 earthquake on 9 May 2019. The F-net MT solution was also high-angle (33°) reverse faulting.
258 The optimal CMT solution indicated a M_w 6.2 low-angle (16°) thrust mechanism. The dip
259 angle from the CMT solution agreed well with that of the Philippine Sea Plate around this
260 earthquake. The synthetic waveforms also corresponded well to observed ones. Although the
261 optimal depth (26 km) was determined to be close to the upper surface of the Philippine Sea
262 Plate (approximately 27 km), a high VR ($> 80\%$) area was found within a wider depth range
263 (16–32 km). Because the depth of this earthquake was deeper than the 2016 southeast off the
264 Kii Peninsula earthquake, the effects of the low-velocity accretionary prism might not have
265 been so strong. Thus, the depth resolution of the CMT solutions might not be good when
266 compared to the case of the 2016 southeast off the Kii Peninsula earthquake. To constrain the
267 hypocentre depth more sharply, additional data, such as shorter-period (~ 4 s) first-arrival P -
268 wave waveforms, would need to be considered (e.g. Okamoto *et al.* 2018, Takemura *et al.*
269 2018a, Wang & Zhan 2020).

270 Figure 5 shows a comparison of the estimated focal mechanisms for the F-net and our 3D
271 CMT catalogues. Our CMT solutions of onshore earthquakes were not significantly differed
272 from those in the F-net catalogue. However, our CMT solutions differed to those based on 1D
273 analysis. In particular, dip angles and centroid depths of offshore earthquakes—which are
274 important for distinguishing interplate and intraslab earthquakes—were different. This was
275 clearly illustrated in detailed comparisons of seismicity southeast off the Kii Peninsula and
276 off the Hyuga-nada (Figures 6, 7, S4, and S5). The dip angles of offshore earthquakes that
277 occurred outside of onshore seismic arrays were poorly estimated by the conventional 1D
278 CMT inversion due to the lack of the 3D subducting oceanic plate and the accretionary prism
279 (e.g. Takemura *et al.* 2018ab). The comparisons and error estimations of dip angles was
280 illustrated in Figures 9 and 10. The comparison of spatial distributions of CMT solutions with
281 the GCMT catalogue is also illustrated in Figure S3.

282 We focused our attention on seismicity southeast off the Kii Peninsula and the Hyuga-nada

283 (local names are illustrated in Figure 1), where seismic activities are relatively high in the
284 Nankai subduction zone. Figure 6 shows spatial distributions of the CMT solutions southeast
285 off the Kii Peninsula. We also plotted shallow VLFs in the catalogue of Takemura *et al.*
286 (2019b) as grey focal spheres. Shallow VLFs, which were characterised by low-angle thrust
287 faulting, were concentrated near the trench. In the region with shallow VLFE active, low-
288 angle thrust type CMT solution at depths of 5-10 km, which suggests seismic slip on the plate
289 boundary, was not estimated. On the down-dip side of the shallow VLFE region, a low-angle
290 thrust faulting mechanism was estimated at a depth near the plate boundary (along profile A
291 in Figure 6). This earthquake is the 2016 southeast off the Kii Peninsula earthquake (Figure
292 3). Almost all of the other earthquakes plotted in Figure 6 are aftershocks of the 2004 M_w 7.5
293 intraslab earthquake that occurred on 5 September 2004 southeast off the Kii Peninsula. Our
294 CMT solutions of these aftershocks were separately distributed at two depths within the
295 oceanic crust and mantle (10–15 and 20–30 km depths). This separation corresponded well to
296 the hypocentre depth distributions of the aftershocks of the M_w 7.5 earthquake as determined
297 using ocean-bottom seismometers (e.g., Nakano *et al.* 2015, Sakai *et al.* 2005). On the other
298 hand, almost all the centroid depths of the F-net solutions were concentrated within the
299 accretionary prism, crust and oceanic crust (5–15 km depths; Figure S3). According to
300 comparisons with the detail hypocentre distributions in this region, even for earthquakes near
301 the trough axis, our CMT method provided better constraints for centroid depths, compared
302 to the 1D F-net MT solutions.

303 Figure 7 shows the spatial distribution of CMT solutions around the Hyuga-nada region.
304 Our CMT solutions characterised by low-angle thrust faulting mechanisms were distributed
305 across the region with average slip rates of approximately 20–40 mm/yr as inferred from
306 small repeating earthquakes (e.g., Yamashita *et al.* 2012). The optimal centroid depths of such
307 thrust solutions were concentrated around the plate boundary (profiles B and C in Figure 7).
308 The distribution of our CMT solutions was agreed with that derived from onshore and
309 temporal offshore seismometers (Tahara *et al.* 2008). The 3D CMT solutions, especially for
310 depths and low-angle thrust faulting mechanisms, corresponded to the areas of detected
311 repeating earthquakes (Yamashita *et al.* 2012). Our 3D CMT also well worked in this region.
312 The dip angles of the F-net MT solutions at depths around the plate boundary were slightly
313 higher than those of the plate boundary, as shown in Figure S4. The centroid depths of the F-
314 net catalogue were also slightly deeper than the depths of the plate boundary. These also
315 might have been due to a lack of 3D geometry of the subducting oceanic plate in the 1D

316 analysis.

317 To evaluate differences between 3D CMT and F-net MT solutions, we calculated
318 correlation coefficients of *P*-wave radiation patterns (e.g., Helffrich 1997, Kuge &
319 Kawakatsu 1993) between two catalogues. We also calculated differences of estimated
320 centroid depths from corresponding F-net solutions. Figure 8 shows the spatial distribution of
321 correlation coefficients of *P*-wave radiation patterns and depth differences between our CMT
322 and F-net MT catalogues. The values of correlation coefficients of offshore earthquakes
323 (enclosed by dashed lines in Figure 8a) were widely distributed. Centroid depths of offshore
324 earthquakes were also different from those of the F-net catalogue. Other earthquakes, which
325 occurred in onshore regions or had good station coverages, have good similarities and small
326 depth differences. The rigidity of the 3D model complicatedly depends on the centroid
327 location, and consequently depth shifts could cause shifts of moment magnitudes from the F-
328 net catalogue (Figure S1).

329 The parameter of the dip angle is important for distinguishing earthquake types. In the
330 Nankai subduction zone, because megathrust earthquakes have repeatedly occurred,
331 seismicity of interplate earthquakes is important. We selected low-angle thrust faulting
332 solutions at depths around the plate boundary from our 3D CMT catalogue. These selected
333 events could be interpreted as seismic slips on the plate boundary. Figure 9 shows a
334 comparison of dip angles between the Philippine Sea plate and suggestive interplate
335 earthquakes from the 3D CMT catalogue. We also compared dip angles of corresponding
336 earthquakes in the F-net MT and GCMT catalogues. Although dip angles of F-net catalogues
337 were higher angles compared to the Philippine Sea plate, our CMT solutions well correlated
338 with dip angles of the plate boundary. Those of the GCMT catalogue roughly corresponded to
339 dip angles of the Philippine Sea plate, but our solutions showed better agreements. The
340 teleseismic CMT solutions are generally robust but regional 3D CMT could provide better
341 constraints of dip angles.

342 We also calculated the VRs between observed and synthetic displacement waveforms to
343 discuss estimation errors of dip angles for offshore earthquakes. Synthetic displacement
344 waveforms were calculated from 3D Green's functions, assuming double-couple point
345 sources and fixing hypocentre locations and seismic moments. Figure 10 shows spatial
346 distributions of VRs for the 2016 southeast off Kii Peninsula earthquake and the 2019 Hyuga-
347 nada earthquake. Clear trade-offs between strike and rake angles appeared in the strike-rake
348 plane (upper panels). We confirmed that higher VR values ($> 75\%$) only appeared in the

349 regions with dip angles of 5-15° and 10-20° for both earthquakes. Thus, our 3D CMT
350 provides constraints of dip angles with uncertainties of approximately $\pm 5^\circ$.

351

352 **4. Discussion**

353 **4.1. Slip behaviours on the plate boundary along the Nankai Trough**

354 In order to discuss slip behaviour on the plate boundary, Figure 11 shows the spatial
355 distribution of slow earthquakes and earthquakes with low-angle ($< 25^\circ$) thrust faulting
356 solutions at depths around the plate boundary along the Nankai Trough. The large coseismic
357 slip area of the 1968 M_w 7.5 earthquake (Yagi *et al.* 1998) is indicated by the blue area in
358 Figure 11. The cumulative deep SSE slips in each grid were determined by summing slip of
359 each SSE in each catalogue (Nishimura *et al.* 2013, Takagi *et al.* 2016, 2019). We then
360 evaluated the SSE slip rates by dividing the cumulative SSE slip at each grid by the analysis
361 period of each catalogue. The SSE slip rate indicates the activity of deep slow earthquakes.
362 We did not calculate SSE slip rates for shallow SSEs reported by Yokota & Ishikawa (2020)
363 because the number of detected events was still too low at each region. For similar reasons,
364 the long-term SSEs off the Kii Channel (Kobayashi 2014) and Tokai (Miyazaki *et al.* 2006)
365 regions were also excluded from the SSE slip rate calculation. Thus, we plotted the fault
366 configurations or large slip areas of long-term SSEs and shallow SSEs. We also plotted
367 shallow LFTs (Yamashita *et al.* 2015) and shallow VLFs (Takemura *et al.* 2019c) as
368 indicators of shallow slow earthquake activity. The spatial distribution of slip-deficit rates
369 from GNSS and GNSS-A observations by Noda *et al.* (2018), is plotted using blue contour
370 lines in Figure 11.

371 At deeper depths (30–40 km), deep slow earthquakes were active, especially in areas with
372 high SSE slip rates, but no interplate regular earthquakes were found. Although SSEs were
373 not removed in the slip-deficit rate estimation of Noda *et al.* (2018)—except for long-term
374 SSEs at the Bungo Channel—the regions with deep SSEs were characterised by low (20–40
375 mm/y) slip-deficit rates. At shallower depths (< 30 km) in the offshore region, regular
376 earthquakes, slow earthquakes, and high (> 60 mm/y) slip-deficit zones were separated from
377 each other. Similar separation of the repeating earthquakes, slow earthquakes, and large
378 coseismic slip areas of megathrust earthquakes at shallower depths were observed in the
379 regions of Tohoku (e.g., Nishikawa *et al.* 2019), Central Ecuador (e.g., Vaca *et al.* 2018) and
380 Costa Rica (e.g., Dixon *et al.* 2014). In particular, Nishikawa *et al.* (2019) pointed out that
381 slow earthquakes were complementarily distributed in the regions surrounding the large

382 coseismic slip area of the 2011 M_w 9.0 Tohoku earthquake. Takemura *et al.* (2019c) pointed
383 out that shallow, slow earthquakes cluster or migrate due to the existence of pore fluid in the
384 transitional regions between high-strength and low-strength zones of the plate boundary.
385 According to these previous studies and our observations, we suggest that the observed
386 separation between slip behaviours on the plate boundary along the Nankai Trough are
387 related to the heterogeneous distribution of effective strengths on the plate boundary, which is
388 controlled by the frictional coefficient, pore fluid pressure, and normal stress.

389

390 **4.2. Regional 3D CMT inversions for the M_w 7.2 and 7.5 earthquakes southeast off the** 391 **Kii Peninsula**

392 We conducted 3D CMT inversions of offshore earthquakes with M_w of 4.3–6.5. During
393 the analysis period (April 2004 to August 2019), M_w 7.2 and 7.5 intraslab earthquakes occurred
394 southeast off the Kii Peninsula on 5 September 2004. Because typical M_w 7 class earthquakes
395 have rupture durations of 30–50 s and fault areas of 1000–5000 km² (e.g. Kanamori & Brodsky
396 2004), precise source parameter estimation for such earthquakes is difficult based on our
397 assumptions of the CMT inversion. Despite these disadvantages, the rapid estimation of CMT
398 solution for these large earthquakes is important for disaster mitigation, such as a CMT-based
399 tsunami warning system. We, therefore, tested the our simple CMT inversion for the M_w 7.2
400 and 7.5 southeast off the Kii Peninsula earthquakes. Because amplitude saturation of F-net
401 broadband seismometers occurs for regional large earthquakes, we used F-net strong motion
402 seismometers, which have a large clip level and a similar frequency response to STS-2
403 seismometers for periods less than 100 s. We selected F-net stations with distances of 200–500
404 km from the initial epicentre, which were slightly farther than for the original CMT settings
405 (100–400 km).

406 Figures 12 and 13 show the results of CMT inversions for the M_w 7.2 and 7.5 earthquakes
407 southeast off the Kii Peninsula, respectively. Detailed estimated parameters are also listed in
408 Table S2. Signal-to-noise ratios were enough high compared to smaller ($M_w < 4.5$)
409 earthquakes in this study but the VRs were low compared to those of moderate earthquakes.
410 The synthetic waveforms roughly corresponded to the observed ones (Figures 12b and 13b).
411 Due to the assumptions of a point source and simple-source time function, detailed
412 characteristics of the observed waveforms were not successfully reproduced. Furthermore,
413 the high (> 66%) VR areas were wider than the CMT results for moderate earthquakes within
414 the same region (Figure 3). The estimated deviatoric components were very similar to those
415 in the GCMT catalogue, but, especially in the result of the M_w 7.2 earthquake, a large
416 isotropic component appeared. Waveform fitting and large non-double couple components

417 suggest the likely complexity of the rupture processes and the source extents for the M_w 7.2
418 and 7.5 earthquakes. Estimated moment magnitudes were slightly smaller than those of the
419 GCMT catalogue as a result of analysed period and the deeper centroid depths. Our analysed
420 period was not enough longer than rupture durations of M_w 7 earthquakes. However, the
421 regional 3D CMT method provides better constraints of dips and depths for offshore
422 earthquakes compared to 1D CMT systems (Figures 3, 4, 5, 6, and 9), and our 3D grid search
423 required only 15-20 minutes. These points are good advantages for CMT-based tsunami
424 prediction systems (e.g. Inazu *et al.* 2016, Reymond *et al.* 2012). To obtain more accurate
425 solutions, the CMT method with various durations (e.g., Takemura *et al.* 2019b) or
426 deconvolution method (e.g., Vallée *et al.* 2011) should be implemented. Such sophisticated
427 methods require more time to obtain solutions.

428 We compared our CMT result for the M_w 7.2 earthquake with the finite-fault model
429 (Okuwaki & Yagi 2018) conducted using teleseismic records based on Yagi & Fukahata
430 (2011). Our horizontal centroid location was very close to an area with large (> 3 m)
431 coseismic slips (Figure 14). The horizontal location of the dominant slip and centroid
432 locations of the 3D CMT solution were shared. The centroid location was also agreed with
433 that estimated by tsunami record (Satake *et al.* 2005). Thus, we think that the centroid
434 location of the M_w 7.2 earthquake was well constrained by our 3D CMT method. The depths
435 of such large coseismic slips in the finite fault model ranged from 9 to 18 km but the optimal
436 centroid depth of the 3D CMT inversion was 26 km. The depth difference could be originated
437 from the regional 3D heterogeneities (accretionary prism, bathymetry change, and subducting
438 plate). According to the hypocentre determinations derived using ocean-bottom seismometers
439 (Nakano *et al.* 2015, Sakai *et al.* 2005), the hypocentres of aftershocks due to the M_w 7.5
440 earthquake were distributed at depths of approximately 10–30 km. We also tested the centroid
441 depth and large isotropic components by our 3D CMT inversion. By using simulated
442 seismograms of the finite-fault model (Okuwaki & Yagi 2018) as observed seismograms, we
443 conducted CMT inversion of the simulated M_w 7.2 intraslab earthquake (Figure S6). The
444 centroid location and depth well corresponded to the large slip area of the finite-fault model.
445 The large isotropic component was also estimated. Thus, large non-double couple
446 components suggest the likely complexity of the rupture processes and the source extents for
447 the finite-fault model of the M_w 7.2 earthquake. Based on the hypocentre distribution of
448 aftershocks, the fault dimensions of the M_w 7.2 earthquake, and synthetic test, we considered
449 that the extension of seismic slips at depths of approximately 26 km might be possible.

450 The detailed rupture processes of the M_w 7.2 and 7.5 earthquakes remain unclear. The
451 regional seismic data and 3D Green's functions may provide additional constraints for large
452 offshore earthquakes. The finite fault modelling based on the 3D Green's functions is an
453 important but challenging issue that requires particular attention in future studies.

454

455 **5. Conclusion**

456 We conducted 3D CMT inversions of moderate earthquakes along the Nankai Trough
457 using the regional 3D Green's function dataset. By comparing 3D CMT solutions with those
458 in the F-net catalogue, large differences in focal mechanisms and centroid depths were found
459 for offshore earthquakes. These differences could be caused by 3D offshore heterogeneities,
460 such as the low-velocity accretionary prism and subducting Philippine Sea plate. Onshore
461 MT inversion using a simple 1D Earth model could provide incorrect estimations due to
462 offshore heterogeneities and station coverage. By introducing the effects of such 3D
463 heterogeneities, the 3D CMT solutions for offshore earthquakes practically agreed with
464 hypocentre distributions determined by ocean-bottom seismometers. Furthermore, our CMT
465 method based on onshore seismograms provided better constrained focal mechanisms and
466 centroid depths compared to the F-net MT catalogue. We also compared our CMT solutions
467 with those of the GCMT catalogue. The teleseismic CMT solutions are generally robust but
468 regional 3D CMT could provide better constraints of dip angles. The regional 3D CMT
469 catalogue contains more earthquakes compared to the GCMT catalogue, where earthquakes
470 with $M_w >$ about 5 are only listed. To investigate detailed decade-scale seismicity in a certain
471 region, CMT inversion incorporating regional 3D velocity model should be required.

472 Although no suggestive interplate earthquakes are listed in the 1D catalogue, some low-
473 angle thrust faulting solutions at depths around the plate boundary were confirmed by our 3D
474 CMT catalogue. These earthquakes could be interpreted as interplate earthquakes. By using
475 our 3D CMT catalogue and previously published slow earthquake models, we illustrated the
476 spatial distribution of slip behaviours on the plate boundary along the Nankai Trough.

477 Regular interplate earthquakes and slow earthquakes occur within different segments on the
478 plate boundary. These separated distributions might reflect the heterogeneous distribution of
479 effective strength on the plate boundary. The gap zones, where no regular interplate and slow
480 earthquakes occurred, were found in the Nankai, Tonankai, and Tokai regions. These were the
481 regions with large (> 60 mm/y) slip-deficit rates, where the plate boundary can be strongly
482 coupled.

483 The regional CMT inversion of earthquakes with $M_w > 7$ was generally difficult due to
484 their fault size and the amplitude saturation of the broadband sensors. CMT inversions for the
485 2004 M_w 7.2 and 7.5 intraslab earthquakes southeast of the Kii Peninsula were performed
486 using the regional broadband strong motion sensors of F-net. Although signal-to-noise ratios
487 of the observed displacements were good enough, the waveform fittings of the M_w 7.2 and
488 7.5 intraslab earthquakes were not good compared to those of typical moderate earthquakes
489 due to fault sizes and the rupture complexity. However, the centroid location was agreed with
490 that estimated by tsunami record and focal mechanism could be constrained. These points and
491 rapid focal mechanism estimation are good advantages for CMT-based tsunami warning
492 systems.

493

494 **Acknowledgements**

495 F-net waveform data and the F-net MT catalogue are available via the website of the National
496 Research Institute for Earth Science and Disaster Resilience
497 (<https://doi.org/10.17598/NIED.0005>). Bathymetric depth data was obtained from ETOPO1
498 (Amante & Eakins 2009). OpenSWPC software (Maeda *et al.* 2017) and the 3D model of
499 Koketsu *et al.* (2012) were obtained from <https://github.com/takuto-maeda/OpenSWPC> and
500 https://www.jishin.go.jp/evaluation/seismic_hazard_map/lpshm/12_choshuki_dat/,
501 respectively. Generic Mapping Tools (Wessel *et al.* 2013) and Seismic Analysis Code (SAC;
502 Helffrich *et al.* 2013) were used to make the figures and when conducting the signal
503 processing work, respectively. The catalogue of slow earthquakes (Nishimura *et al.* 2013,
504 Takagi *et al.* 2016, Yamashita *et al.* 2015) was downloaded from the Slow Earthquake
505 Database website (Kano *et al.* 2018; <http://www-solid.eps.s.u-tokyo.ac.jp/~sloweql/>). Our
506 CMT catalogue and CMT results of assumed source grids for each earthquake are available
507 from <https://doi.org/10.5281/zenodo.3674161>. The FDM simulations of seismic wave
508 propagation were conducted on the computer system of the Earthquake and Volcano
509 Information Center at the Earthquake Research Institute, the University of Tokyo. This study
510 was supported by the Japan Society for the Promotion of Science (JSPS) KAKENHI Grant
511 Numbers 17K14382 under the Grant-in-Aid for Young Scientists (B) and 19H04626 in
512 Scientific Research under Innovative Areas ‘Science of Slow Earthquakes’. We also thank
513 two anonymous reviewers and Editor Prof. J. Virieux for careful reviewing and constructive
514 comments, which have helped to improve the manuscript.

515

516 **References**

517 Aki, K. & Richards, P. (2002) *Quantitative Seismology*, 2nd ed., University Science Books.
518 Retrieved from https://www.ldeo.columbia.edu/~richards/Aki_Richards.html

- 519 Amante, C. & Eakins, B.W. (2009) ETOPO1 1 arc-minute global relief model: Procedures,
520 data sources and analysis. NOAA Technical Memorandum NESDIS NGDC-24. *NOAA*
521 *Tech. Memo. NESDIS NGDC-24. Natl. Geophys. Data Center, NOAA*, 19.
522 doi:10.7289/V5C8276M
- 523 Ando, M. (1975) Source mechanisms and tectonic significance of historical earthquakes
524 along the Nankai trough, Japan. *Tectonophysics*, **27**, 119–140. doi:10.1016/0040-
525 1951(75)90102-X
- 526 Dixon, T.H., Jiang, Y., Malservisi, R., McCaffrey, R., Voss, N., Protti, M. & Gonzalez, V.
527 (2014) Earthquake and tsunami forecasts: Relation of slow slip events to subsequent
528 earthquake rupture. *Proc. Natl. Acad. Sci.*, **111**, 17039–17044.
529 doi:10.1073/pnas.1412299111
- 530 Dziewonski, A.M., Chou, T.-A. & Woodhouse, J.H. (1981) Determination of earthquake
531 source parameters from waveform data for studies of global and regional seismicity. *J.*
532 *Geophys. Res. Solid Earth*, **86**, 2825–2852. doi:10.1029/JB086iB04p02825
- 533 Eberhart-Phillips, D., Reyners, M., Bannister, S., Chadwick, M. & Ellis, S. (2010)
534 Establishing a versatile 3-D seismic velocity model for New Zealand. *Seismol. Res.*
535 *Lett.*, **81**, 992–1000. doi:10.1785/gssrl.81.6.992
- 536 Eisner, L. & Clayton, R.W. (2001) A reciprocity method for multiple-source simulations.
537 *Bull. Seismol. Soc. Am.*, **91**, 553–560. doi:10.1785/0120000222
- 538 Ekström, G., Nettles, M. & Dziewoński, A.M. (2012) The global CMT project 2004-2010:
539 Centroid-moment tensors for 13,017 earthquakes. *Phys. Earth Planet. Inter.*, **200–201**,
540 1–9. doi:10.1016/j.pepi.2012.04.002
- 541 Fukuyama, E., Ishida, M., Dreger, D.S. & Kawai, H. (1998) Automated seismic moment
542 tensor determination by using on-line broadband seismic waveforms. *Zisin*, **51**, 149–
543 156. doi:10.4294/zisin1948.51.1_149
- 544 Gokhberg, A. & Fichtner, A. (2016) Full-waveform inversion on heterogeneous HPC
545 systems. *Comput. Geosci.*, **89**, 260–268, Elsevier. doi:10.1016/j.cageo.2015.12.013
- 546 Gomberg, J. (2018) Cascadia Onshore-Offshore Site Response, Submarine Sediment
547 Mobilization, and Earthquake Recurrence. *J. Geophys. Res. Solid Earth*, **123**, 1381–
548 1404. doi:10.1002/2017JB014985
- 549 Hardebeck, J.L. & Shearer, P.M. (2002) A new method for determining first-motion focal
550 mechanisms. *Bull. Seismol. Soc. Am.*, **92**, 2264–2276. doi:10.1785/0120010200
- 551 Hejrani, B., Tkalčić, H. & Fichtner, A. (2017) Centroid moment tensor catalogue using a 3-D
552 continental scale Earth model: Application to earthquakes in Papua New Guinea and the
553 Solomon Islands. *J. Geophys. Res. Solid Earth*, **122**, 5517–5543.
554 doi:10.1002/2017JB014230
- 555 Helffrich, G., Wookey, J. & Bastow, I. (2013) *The Seismic Analysis Code*, Cambridge:
556 Cambridge University Press. doi:10.1017/CBO9781139547260

- 557 Helffrich, G.R. (1997) How good are routinely determined focal mechanisms? Empirical
558 statistics based on a comparison of Harvard, USGS and ERI moment tensors. *Geophys.*
559 *J. Int.*, **131**, 741–750. doi:10.1111/j.1365-246X.1997.tb06609.x
- 560 Hirose, F., Nakajima, J. & Hasegawa, A. (2008) Three-dimensional seismic velocity structure
561 and configuration of the Philippine Sea slab in southwestern Japan estimated by double-
562 difference tomography. *J. Geophys. Res. Solid Earth*, **113**, 1–26.
563 doi:10.1029/2007JB005274
- 564 Inazu, D., Pulido, N., Fukuyama, E., Saito, T., Senda, J. & Kumagai, H. (2016) Near-field
565 tsunami forecast system based on near real-time seismic moment tensor estimation in the
566 regions of Indonesia, the Philippines, and Chile 4. *Seismology. Earth, Planets Sp.*, **68**,
567 Springer Berlin Heidelberg. doi:10.1186/s40623-016-0445-x
- 568 Ito, Y. & Obara, K. (2006) Dynamic deformation of the accretionary prism excites very low
569 frequency earthquakes. *Geophys. Res. Lett.*, **33**, L02311. doi:10.1029/2005GL025270
- 570 Kamei, R., Pratt, R.G. & Tsuji, T. (2012) Waveform tomography imaging of a megasplay
571 fault system in the seismogenic Nankai subduction zone. *Earth Planet. Sci. Lett.*, **317**–
572 **318**, 343–353, Elsevier B.V. doi:10.1016/j.epsl.2011.10.042
- 573 Kanamori, H. & Brodsky, E.E. (2004) The physics of earthquakes. *Reports Prog. Phys.*, **67**,
574 1429–1496. doi:10.1088/0034-4885/67/8/R03
- 575 Kanamori, H. & Rivera, L. (2008) Source inversion of W phase: Speeding up seismic
576 tsunami warning. *Geophys. J. Int.*, **175**, 222–238. doi:10.1111/j.1365-
577 246X.2008.03887.x
- 578 Kaneko, Y., Ito, Y., Chow, B., Wallace, L.M., Tape, C., Grapenthin, R., D’Anastasio, E., *et*
579 *al.* (2019) Ultra-long Duration of Seismic Ground Motion Arising From a Thick, Low-
580 Velocity Sedimentary Wedge. *J. Geophys. Res. Solid Earth*, **124**, 10347–10359.
581 doi:10.1029/2019JB017795
- 582 Kano, M., Aso, N., Matsuzawa, T., Ide, S., Annoura, S., Arai, R., Baba, S., *et al.* (2018)
583 Development of a Slow Earthquake Database. *Seismol. Res. Lett.*, **89**, 1566–1575.
584 doi:10.1785/0220180021
- 585 Kikuchi, M. & Kanamori, H. (1991) Inversion of complex body waves-III. *Bull. Seism. Soc.*
586 *Am.*, **81**, 2335–2350. Retrieved from
587 [https://pubs.geoscienceworld.org/ssa/bssa/article/81/6/2335/102472/inversion-of-](https://pubs.geoscienceworld.org/ssa/bssa/article/81/6/2335/102472/inversion-of-complex-body-waves-iii)
588 [complex-body-waves-iii](https://pubs.geoscienceworld.org/ssa/bssa/article/81/6/2335/102472/inversion-of-complex-body-waves-iii)
- 589 Kimura, T., Murakami, H. & Matsumoto, T. (2015) Systematic monitoring of instrumentation
590 health in high-density broadband seismic networks. *Earth, Planets Sp.*, **67**, 55.
591 doi:10.1186/s40623-015-0226-y
- 592 Kobayashi, A. (2014) A long-term slow slip event from 1996 to 1997 in the Kii Channel,
593 Japan. *Earth, Planets Sp.*, **66**, 1–7. doi:10.1186/1880-5981-66-9
- 594 Koketsu, K., Miyake, H. & Suzuki, H. (2012) Japan Integrated Velocity Structure Model

- 595 Version 1. *Proc. 15th World Conf. Earthq. Eng.*, 1–4. Retrieved from
596 http://www.iitk.ac.in/nicee/wcee/article/WCEE2012_1773.pdf
- 597 Kubo, A., Fukuyama, E., Kawai, H. & Nonomura, K. (2002) NIED seismic moment tensor
598 catalogue for regional earthquakes around Japan: Quality test and application.
599 *Tectonophysics*, **356**, 23–48. doi:10.1016/S0040-1951(02)00375-X
- 600 Kubota, T., Suzuki, W., Nakamura, T., Chikasada, N.Y., Aoi, S., Takahashi, N. & Hino, R.
601 (2018) Tsunami source inversion using time-derivative waveform of offshore pressure
602 records to reduce effects of non-tsunami components. *Geophys. J. Int.*, **215**, 1200–1214,
603 Oxford University Press. doi:10.1093/GJI/GGY345
- 604 Kuge, K. & Kawakatsu, H. (1993) Significance of non-double couple components of deep
605 and intermediate-depth earthquakes: implications from moment tensor inversions of
606 long-period seismic waves. *Phys. Earth Planet. Inter.*, **75**, 243–266. doi:10.1016/0031-
607 9201(93)90004-S
- 608 Lee, S.-J., Liang, W.T., Cheng, H.W., Tu, F.S., Ma, K.F., Tsuruoka, H., Kawakatsu, H., *et al.*
609 (2013) Towards real-time regional earthquake simulation I: Real-time moment tensor
610 monitoring (RMT) for regional events in Taiwan. *Geophys. J. Int.*, **196**, 432–446.
611 doi:10.1093/gji/ggt371
- 612 Maeda, T., Takemura, S. & Furumura, T. (2017) OpenSWPC: an open-source integrated
613 parallel simulation code for modeling seismic wave propagation in 3D heterogeneous
614 viscoelastic media. *Earth, Planets Sp.*, **69**, 102, Springer Berlin Heidelberg.
615 doi:10.1186/s40623-017-0687-2
- 616 Miyazaki, S., Segall, P., McGuire, J.J., Kato, T. & Hatanaka, Y. (2006) Spatial and temporal
617 evolution of stress and slip rate during the 2000 Tokai slow earthquake. *J. Geophys. Res.*
618 *Solid Earth*, **111**, 1–17. doi:10.1029/2004JB003426
- 619 Nakanishi, A., Kodaira, S., Park, J.-O. & Kaneda, Y. (2002) Deformable backstop as seaward
620 end of coseismic slip in the Nankai Trough seismogenic zone. *Earth Planet. Sci. Lett.*,
621 **203**, 255–263. doi:10.1016/S0012-821X(02)00866-X
- 622 Nakano, M., Nakamura, T. & Kaneda, Y. (2015) Hypocenters in the Nankai Trough
623 determined by using data from both ocean-bottom and land seismic networks and a 3D
624 velocity structure model: Implications for seismotectonic activity. *Bull. Seismol. Soc.*
625 *Am.*, **105**, 1594–1605. doi:10.1785/0120140309
- 626 Nakano, M., Hyodo, M., Nakanishi, A., Yamashita, M., Hori, T., Kamiya, S., Suzuki, K., *et*
627 *al.* (2018a) The 2016 Mw 5.9 earthquake off the southeastern coast of Mie Prefecture as
628 an indicator of preparatory processes of the next Nankai Trough megathrust earthquake.
629 *Prog. Earth Planet. Sci.*, **5**, 30, Progress in Earth and Planetary Science.
630 doi:10.1186/s40645-018-0188-3
- 631 Nakano, M., Hori, T., Araki, E., Kodaira, S. & Ide, S. (2018b) Shallow very-low-frequency
632 earthquakes accompany slow slip events in the Nankai subduction zone. *Nat. Commun.*,

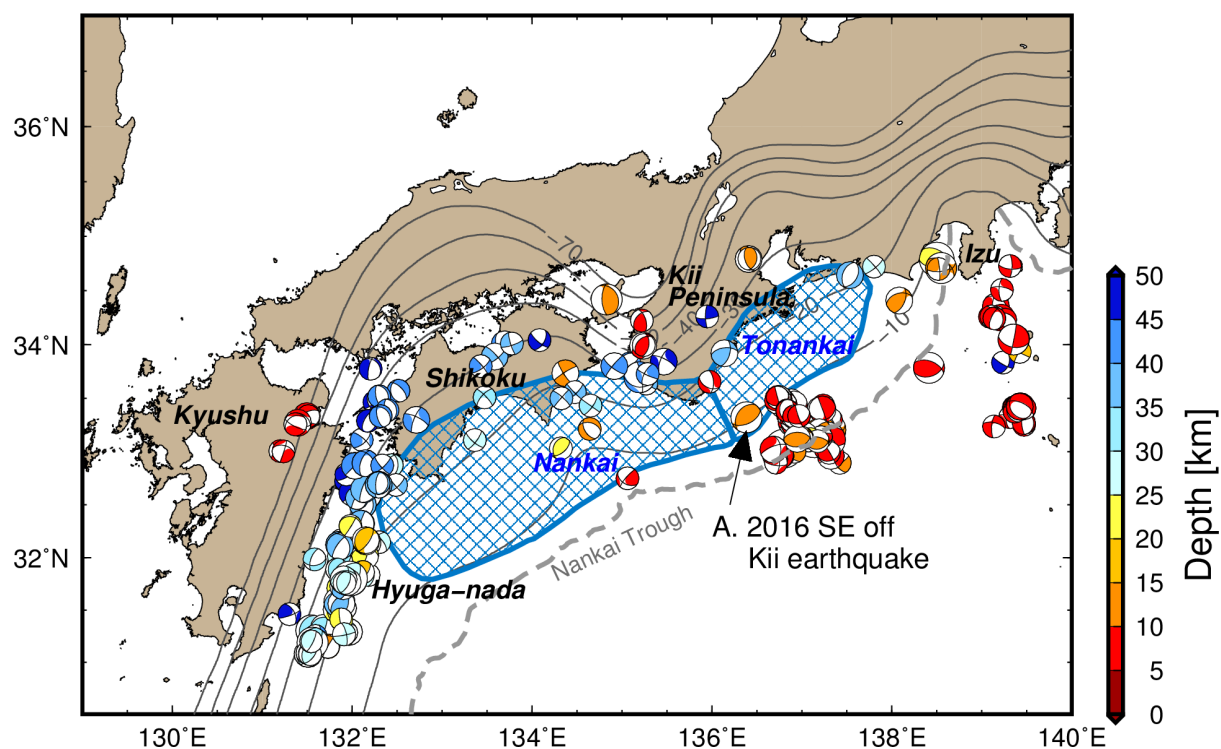
- 633 9, 984. doi:10.1038/s41467-018-03431-5
- 634 National Research Institute for Earth Science and Disaster Resilience. (2019) NIED F-net.
635 *Natl. Res. Inst. Earth Sci. Disaster Resil.* doi:10.17598/NIED.0005
- 636 Nishikawa, T., Matsuzawa, T., Ohta, K., Uchida, N., Nishimura, T. & Ide, S. (2019) The
637 slow earthquake spectrum in the Japan Trench illuminated by the S-net seafloor
638 observatories. *Science*, **365**, 808–813. doi:10.1126/science.aax5618
- 639 Nishimura, T., Matsuzawa, T. & Obara, K. (2013) Detection of short-term slow slip events
640 along the Nankai Trough, southwest Japan, using GNSS data. *J. Geophys. Res. Solid*
641 *Earth*, **118**, 3112–3125, Wiley-Blackwell. doi:10.1002/jgrb.50222
- 642 Noda, A., Saito, T. & Fukuyama, E. (2018) Slip-Deficit Rate Distribution Along the Nankai
643 Trough, Southwest Japan, With Elastic Lithosphere and Viscoelastic Asthenosphere. *J.*
644 *Geophys. Res. Solid Earth*, **123**, 8125–8142. doi:10.1029/2018JB015515
- 645 Okada, Y., Kasahara, K., Hori, S., Obara, K., Sekiguchi, S., Fujiwara, H. & Yamamoto, A.
646 (2004) Recent progress of seismic observation networks in Japan —Hi-net, F-net, K-
647 NET and KiK-net—. *Earth, Planets Sp.*, **56**, xv–xxviii. doi:10.1186/BF03353076
- 648 Okamoto, T., Takenaka, H. & Nakamura, T. (2018) Evaluation of accuracy of synthetic
649 waveforms for subduction-zone earthquakes by using a land–ocean unified 3D structure
650 model. *Earth, Planets Sp.*, **70**, Springer Berlin Heidelberg. doi:10.1186/s40623-018-
651 0871-z
- 652 Okuwaki, R. & Yagi, Y. (2018) Seismic source model for the Mw 7.2 2004 Kii peninsula,
653 Japan, earthquake. *Github*. doi:10.5281/zenodo.1493833
- 654 Park, J.-O., Fujie, G., Wijerathne, L., Hori, T., Kodaira, S., Fukao, Y., Moore, G.F., *et al.*
655 (2010) A low-velocity zone with weak reflectivity along the Nankai subduction zone.
656 *Geology*, **38**, 283–286. doi:10.1130/G30205.1
- 657 Ramos-Martínez, J. & McMechan, G.A. (2001) Source-parameter estimation by full
658 waveform inversion in 3D heterogeneous, viscoelastic, anisotropic media. *Bull. Seismol.*
659 *Soc. Am.*, **91**, 276–291. doi:10.1785/0120000017
- 660 Reymond, D., Okal, E.A., Hébert, H. & Bourdet, M. (2012) Rapid forecast of tsunami wave
661 heights from a database of pre-computed simulations, and application during the 2011
662 Tohoku tsunami in French Polynesia. *Geophys. Res. Lett.*, **39**, 1–6.
663 doi:10.1029/2012GL051640
- 664 Saito, T., Noda, A., Yoshida, K. & Tanaka, S. (2018) Shear strain energy change caused by
665 the interplate coupling along the Nankai Trough: An integration analysis using stress
666 tensor inversion and slip deficit inversion. *J. Geophys. Res. Solid Earth*.
667 doi:10.1029/2018JB015839
- 668 Sakai, S., Yamada, T., Shinohara, M., Hagiwara, H., Kanazawa, T., Obana, K., Kodaira, S.,
669 *et al.* (2005) Urgent aftershock observation of the 2004 off the Kii Peninsula earthquake
670 using ocean bottom seismometers. *Earth Planets Sp.*, **57**, 363–368.

- 671 doi:10.1186/BF03352577
- 672 Satake, K., Baba, T., Hirata, K., Iwasaki, S.I., Kato, T., Koshimura, S., Takenaka, J., *et al.*
673 (2005) Tsunami source of the 2004 off the Kii Peninsula earthquakes inferred from
674 offshore tsunami and coastal tide gauges. *Earth, Planets Sp.*, **57**, 173–178.
675 doi:10.1186/BF03351811
- 676 Shapiro, N.M., Campillo, M., Singh, S.K. & Pacheco, J. (1998) Seismic channel waves in the
677 accretionary prism of the Middle America Trench. *Geophys. Res. Lett.*, **25**, 101–104.
678 doi:10.1029/97GL03492
- 679 Shelly, D.R., Hardebeck, J.L., Ellsworth, W.L. & Hill, D.P. (2016) A new strategy for
680 earthquake focal mechanisms using waveform-correlation-derived relative polarities and
681 cluster analysis: Application to the 2014 Long Valley Caldera earthquake swarm. *J.*
682 *Geophys. Res. Solid Earth*, **121**, 8622–8641. doi:10.1002/2016JB013437
- 683 Shiomi, K., Obara, K. & Sato, H. (2006) Moho depth variation beneath southwestern Japan
684 revealed from the velocity structure based on receiver function inversion.
685 *Tectonophysics*, **420**, 205–221. doi:10.1016/j.tecto.2006.01.017
- 686 Storchak, D.A., Giacomo, D. Di, Bondár, I., Engdahl, E.R., Harris, J., Lee, W.H.K. &
687 Villaseñor, A. (2013) Public Release of the ISC – GEM Global Instrumental Earthquake
688 Catalogue (1900 – 2009). doi:10.1785/0220130034
- 689 Tahara, M., Uehira, K., Shimizu, H., Nakada, M., Yamada, T., Mochizuki, K., Shinohara, M.,
690 *et al.* (2008) Seismic velocity structure around the Hyuganada region, Southwest Japan,
691 derived from seismic tomography using land and OBS data and its implications for
692 interplate coupling and vertical crustal uplift. *Phys. Earth Planet. Inter.*, **167**, 19–33.
693 doi:10.1016/j.pepi.2008.02.001
- 694 Takagi, R., Obara, K. & Maeda, T. (2016) Slow slip event within a gap between tremor and
695 locked zones in the Nankai subduction zone. *Geophys. Res. Lett.*, **43**, 1066–1074.
696 doi:10.1002/2015GL066987
- 697 Takagi, R., Uchida, N. & Obara, K. (2019) Along-Strike Variation and Migration of Long-
698 Term Slow Slip Events in the Western Nankai Subduction Zone, Japan. *J. Geophys. Res.*
699 *Solid Earth*, **124**, 3853–3880. doi:10.1029/2018JB016738
- 700 Takemura, S., Shiomi, K., Kimura, T. & Saito, T. (2016) Systematic difference between first
701 - motion and waveform - inversion solutions for shallow offshore earthquakes due to a
702 low - angle dipping slab. *Earth, Planets Sp.*, 1–8, Springer Berlin Heidelberg.
703 doi:10.1186/s40623-016-0527-9
- 704 Takemura, S., Kimura, T., Saito, T., Kubo, H. & Shiomi, K. (2018a) Moment tensor
705 inversion of the 2016 southeast offshore Mie earthquake in the Tonankai region using a
706 three-dimensional velocity structure model: effects of the accretionary prism and
707 subducting oceanic plate. *Earth, Planets Sp.*, **70**, 50, Springer Berlin Heidelberg.
708 doi:10.1186/s40623-018-0819-3

- 709 Takemura, S., Matsuzawa, T., Kimura, T., Tonegawa, T. & Shiomi, K. (2018b) Centroid
710 Moment Tensor Inversion of Shallow Very Low Frequency Earthquakes Off the Kii
711 Peninsula, Japan, Using a Three-Dimensional Velocity Structure Model. *Geophys. Res.
712 Lett.*, **45**, 6450–6458. doi:10.1029/2018GL078455
- 713 Takemura, S., Kubo, H., Tonegawa, T., Saito, T. & Shiomi, K. (2019a) Modeling of Long-
714 Period Ground Motions in the Nankai Subduction Zone: Model Simulation Using the
715 Accretionary Prism Derived from Oceanfloor Local S-Wave Velocity Structures. *Pure
716 Appl. Geophys.*, **176**, 627–647, Birkhauser Verlag AG. doi:10.1007/s00024-018-2013-8
- 717 Takemura, S., Matsuzawa, T., Noda, A., Tonegawa, T., Asano, Y., Kimura, T. & Shiomi, K.
718 (2019b) Structural Characteristics of the Nankai Trough Shallow Plate Boundary
719 Inferred From Shallow Very Low Frequency Earthquakes. *Geophys. Res. Lett.*, **46**,
720 4192–4201, Blackwell Publishing Ltd. doi:10.1029/2019GL082448
- 721 Takemura, S., Noda, A., Kubota, T., Asano, Y., Matsuzawa, T. & Shiomi, K. (2019c)
722 Migrations and Clusters of Shallow Very Low Frequency Earthquakes in the Regions
723 Surrounding Shear Stress Accumulation Peaks Along the Nankai Trough. *Geophys. Res.
724 Lett.*, **46**, 11830–11840. doi:10.1029/2019GL084666
- 725 Terakawa, T. & Matsu'ura, M. (2010) The 3-D tectonic stress fields in and around Japan
726 inverted from centroid moment tensor data of seismic events. *Tectonics*, **29**, 1–14.
727 doi:10.1029/2009TC002626
- 728 Townend, J. & Zoback, M.D. (2006) Stress, strain, and mountain building in central Japan. *J.
729 Geophys. Res. Solid Earth*, **111**, 1–11. doi:10.1029/2005JB003759
- 730 Vaca, S., Vallée, M., Nocquet, J.M., Battaglia, J. & Régnier, M. (2018) Recurrent slow slip
731 events as a barrier to the northward rupture propagation of the 2016 Pedernales
732 earthquake (Central Ecuador). *Tectonophysics*, **724–725**, 80–92, Elsevier.
733 doi:10.1016/j.tecto.2017.12.012
- 734 Vallée, M., Charléty, J., Ferreira, A.M.G., Delouis, B. & Vergoz, J. (2011) SCARDEC: A
735 new technique for the rapid determination of seismic moment magnitude, focal
736 mechanism and source time functions for large earthquakes using body-wave
737 deconvolution. *Geophys. J. Int.*, **184**, 338–358. doi:10.1111/j.1365-246X.2010.04836.x
- 738 Wallace, L.M., Araki, E., Saffer, D., Wang, X., Roesner, A., Kopf, A., Nakanishi, A., *et al.*
739 (2016) Near-field observations of an offshore M w 6.0 earthquake from an integrated
740 seafloor and subseafloor monitoring network at the Nankai Trough, southwest Japan. *J.
741 Geophys. Res. Solid Earth*, **121**, 8338–8351. doi:10.1002/2016JB013417
- 742 Wang, X. & Zhan, Z. (2020) Moving from 1-D to 3-D velocity model: automated waveform-
743 based earthquake moment tensor inversion in the Los Angeles region. *Geophys. J. Int.*,
744 **220**, 218–234. doi:10.1093/gji/ggz435
- 745 Wessel, P., Smith, W.H.F., Scharroo, R., Luis, J. & Wobbe, F. (2013) Generic mapping tools:
746 Improved version released. *Eos (Washington. DC)*, **94**, 409–410.

- 747 doi:10.1002/2013EO450001
- 748 Yagi, Y., Kikuchi, M., Yoshida, S. & Yamanaka, Y. (1998) Source Process of the Hyuga-
749 nada Earthquake of April 1, 1968 (MJMA 7.5), and its Relationship to the Subsequent
750 Seismicity. *Zisin (Journal Seismol. Soc. Japan. 2nd ser.)*, **51**, 139–148.
751 doi:10.4294/zisin1948.51.1_139
- 752 Yagi, Y. & Fukahata, Y. (2011) Introduction of uncertainty of Green’s function into
753 waveform inversion for seismic source processes. *Geophys. J. Int.*, **186**, 711–720.
754 doi:10.1111/j.1365-246X.2011.05043.x
- 755 Yamashita, Y., Shimizu, H. & Goto, K. (2012) Small repeating earthquake activity, interplate
756 quasi-static slip, and interplate coupling in the Hyuga-nada, southwestern Japan
757 subduction zone. *Geophys. Res. Lett.*, **39**, 1–5. doi:10.1029/2012GL051476
- 758 Yamashita, Y., Yakiwara, H., Asano, Y., Shimizu, H., Uchida, K., Hirano, S., Umakoshi, K.,
759 *et al.* (2015) Migrating tremor off southern Kyushu as evidence for slow slip of a
760 shallow subduction interface. *Science*, **348**, 676–679. doi:10.1126/science.aaa4242
- 761 Yokota, Y. & Ishikawa, T. (2020) Shallow slow slip events along the Nankai Trough detected
762 by GNSS-A. *Sci. Adv.*, **6**, eaay5786. doi:10.1126/sciadv.aay5786
- 763
- 764

765 **Figures**

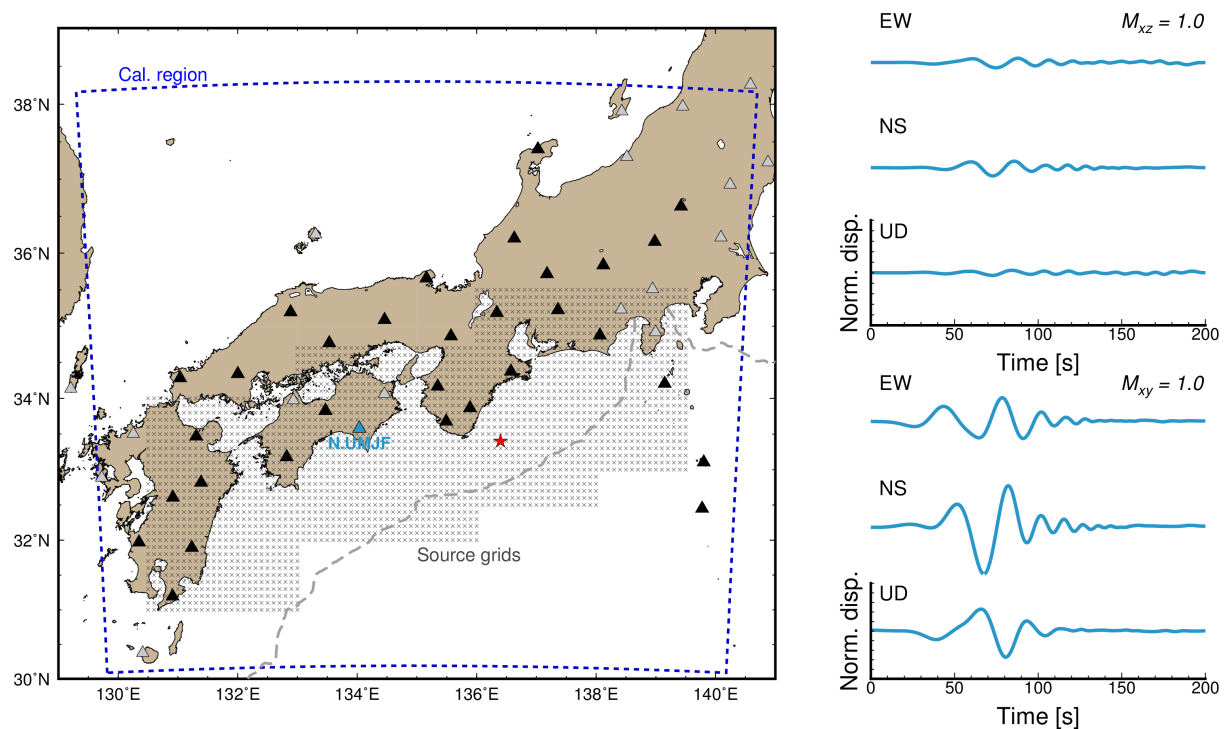


766

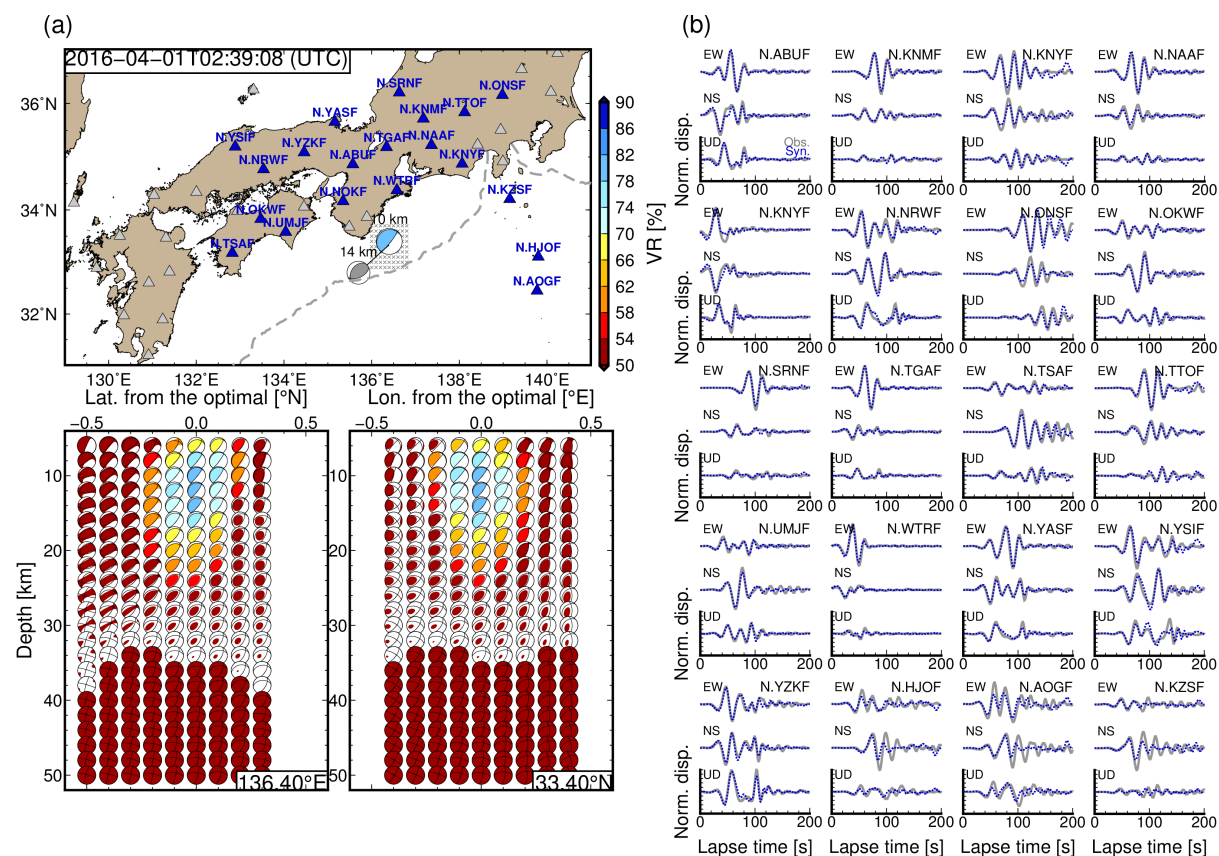
767 Figure 1. Map of the study region. The black contour lines are the iso-depth contour lines of
768 the upper surface of the Philippine Sea Plate of Koketsu *et al.* (2012). Focal mechanisms
769 are the moment tensor (MT) solutions of regular earthquakes with M_w of 4.3–6.5 in the
770 F-net catalogue (Fukuyama *et al.* 1998, Kubo *et al.* 2002) that occurred in the area with
771 latitudes less than 34.8°N , longitudes greater than 131°E , and at depths of less than 50
772 km. The plotted MT solutions range from April 2004 to August 2019. The blue hatched
773 areas represent the expected source region of the Nankai and Tonankai earthquakes
774 (Earthquake Research Committee, 2001, available at:
775 http://www.jishin.go.jp/main/chousa/01sep_nankai/index.htm). The earthquake marked A
776 is the M_w 5.8 southeast off Kii Peninsula earthquake that occurred on 1 April 2016.

777

778



779
780 Figure 2. Calculation settings used in this study were the blue dashed line represents the
781 horizontal coverage of the simulation model region. The triangles and crosses in the map
782 denote the locations of the F-net stations and the assumed source grids, respectively.
783 Green's functions from the source grids to the black-fill and blue-fill triangles were
784 evaluated via reciprocal calculations using OpenSWPC code (Maeda *et al.* 2017). The
785 right-hand panels show examples of filtered displacements of Green's functions from a
786 certain hypocentre (red star, at a depth of 10 km) to the N.UMJF station (blue triangle),
787 whose epicentral distance is 263 km. The filter passed band ranged from 25 to 100 s.
788
789



790

791

792

793

794

795

796

797

798

799

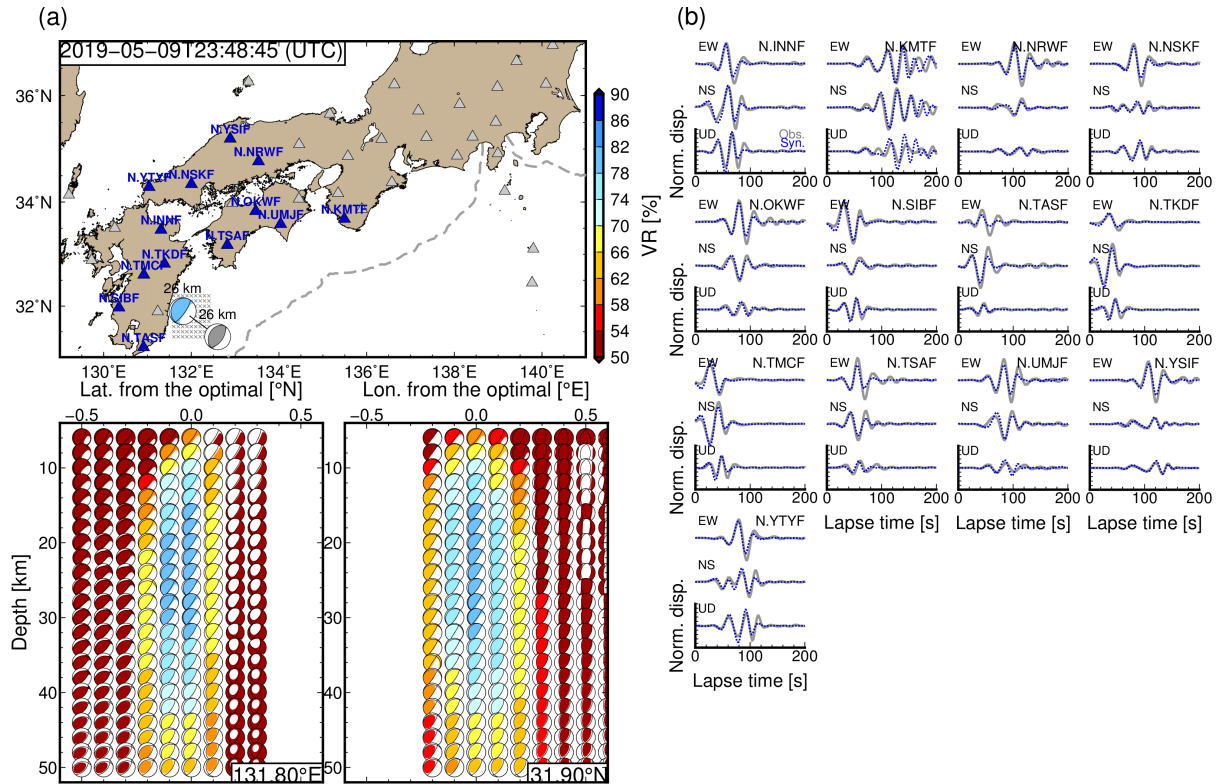
800

801

802

803

Figure 3. CMT results for the southeast off Kii Peninsula earthquake that occurred on 1 April 2016. (a) Locations of the optimal solutions, used stations, and depth variations of optimal solutions at each source grid. Colours of the focal mechanisms reflect values of variance reduction between observed and synthetic displacements for 25–100 s periods. The numbers above the optimal solutions in (a) are the optimal centroid depths. The grey focal mechanism in (a) is the F-net MT solution of this earthquake. (b) Comparisons of observed and synthetic displacements for 25–100 s periods. Grey solid and blue dotted lines are the observed and synthetic seismograms, respectively. Synthetic seismograms were evaluated by assuming the optimal solution. Amplitudes at each station were normalised by the maximum amplitude of both observed and synthetic three-component displacement waveforms. Detailed source parameters are listed in Table S1.



804

805 Figure 4. CMT results for the Hyuga-nada earthquake that occurred on 9 May 2019. (a)

806

Locations of the optimal solutions, used stations, and depth variations of optimal

807

solutions at each source grid. Colours of the focal mechanisms reflect values of variance

808

reduction between observed and synthetic displacements for 25–100 s periods. The

809

numbers above the optimal solutions in (a) are the optimal centroid depths. The grey

810

focal mechanism in (a) is the F-net MT solution of this earthquake. (b) Comparisons of

811

observed and synthetic displacements for 25–100 s periods. Grey solid and blue dotted

812

lines are the observed and synthetic seismograms, respectively. Synthetic seismograms

813

were evaluated by assuming the optimal solution. Amplitudes at each station were

814

normalised by the maximum amplitude of both observed and synthetic three-component

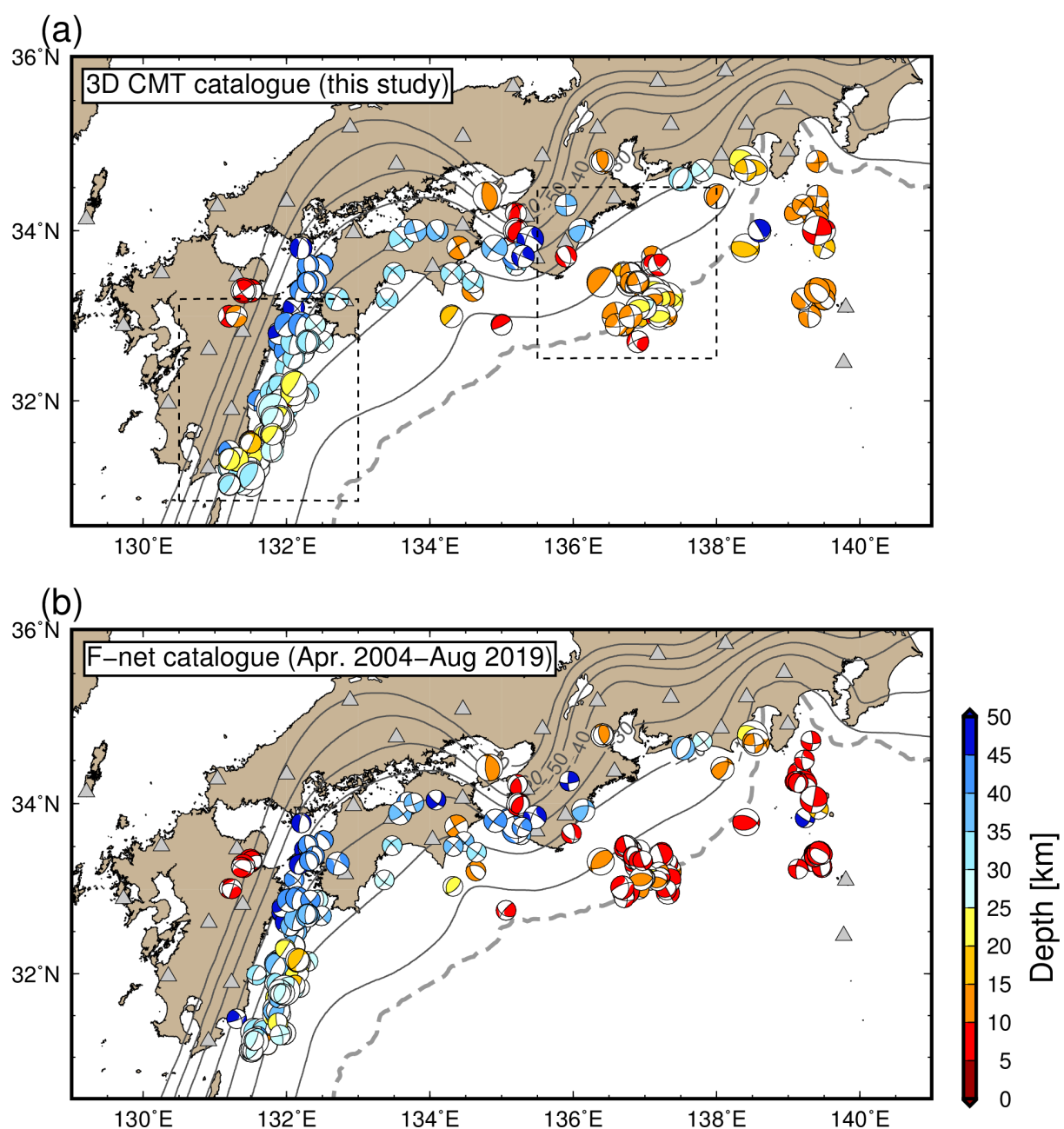
815

displacement waveforms. Detailed source parameters are listed in Table S1.

816

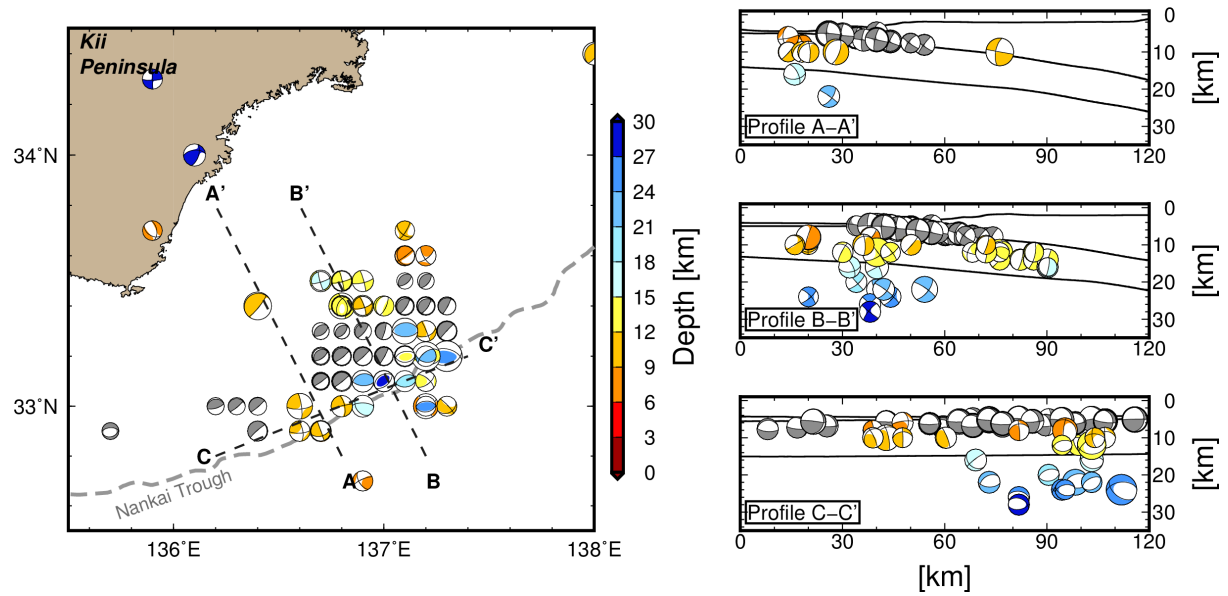
817

818



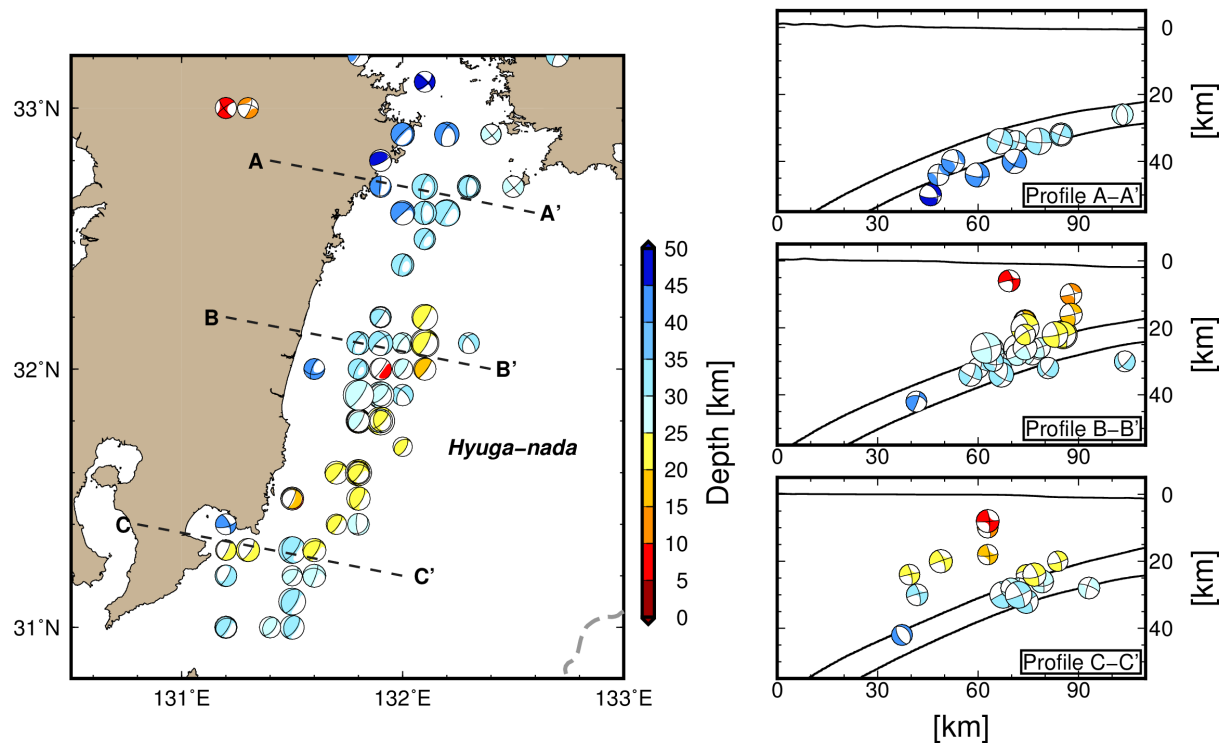
819
820 Figure 5. Comparisons of estimated CMT solutions between the (a) 3D CMT and (b) F-net
821 MT catalogues. Colours of focal mechanisms represent the centroid depths of each
822 solution. Detailed source parameters of our 3D CMT solutions are listed in Table S1. The
823 regions enclosed by the dashed lines in (a) are enlarged in Figures 6 and 7.

824
825
826



827

828 Figure 6. Spatial distribution of the CMT solutions southeast of the Kii Peninsula. Coloured
829 focal mechanisms are our CMT solutions. Grey focal mechanisms are the CMT solutions
830 of shallow VLFs (Takemura, Shunsuke, Matsuzawa, *et al.* 2019). The right-hand panels
831 show cross-sections along profiles A-A', B-B' and C-C'. The bathymetry of ETOPO1
832 (Amante & Eakins 2009), the upper surface, and oceanic Moho of the Philippine Sea
833 Plate (Koketsu *et al.* 2012) along each profile are plotted in the right-hand panels.

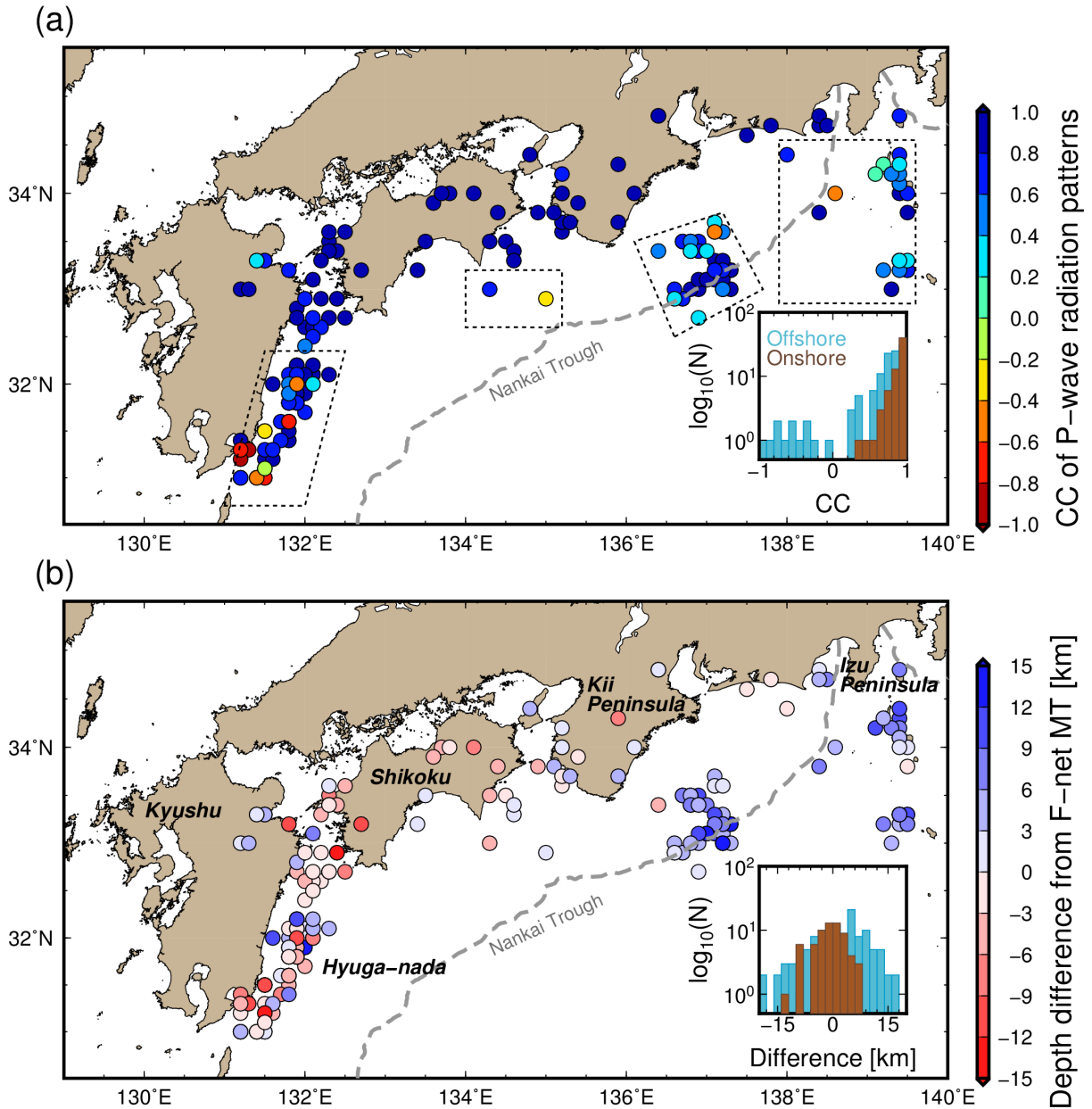


834

835 Figure 7. CMT results for the Hyuga-nada region. Coloured focal mechanisms are our CMT
836 solutions. The right-hand panels show cross-sections along profiles A-A', B-B' and C-C'.

837 The bathymetry of ETOPO1 (Amante & Eakins 2009), the upper surface, and oceanic
 838 Moho of the Philippine Sea Plate (Koketsu *et al.* 2012) along each profile are plotted in
 839 the right-hand panels.

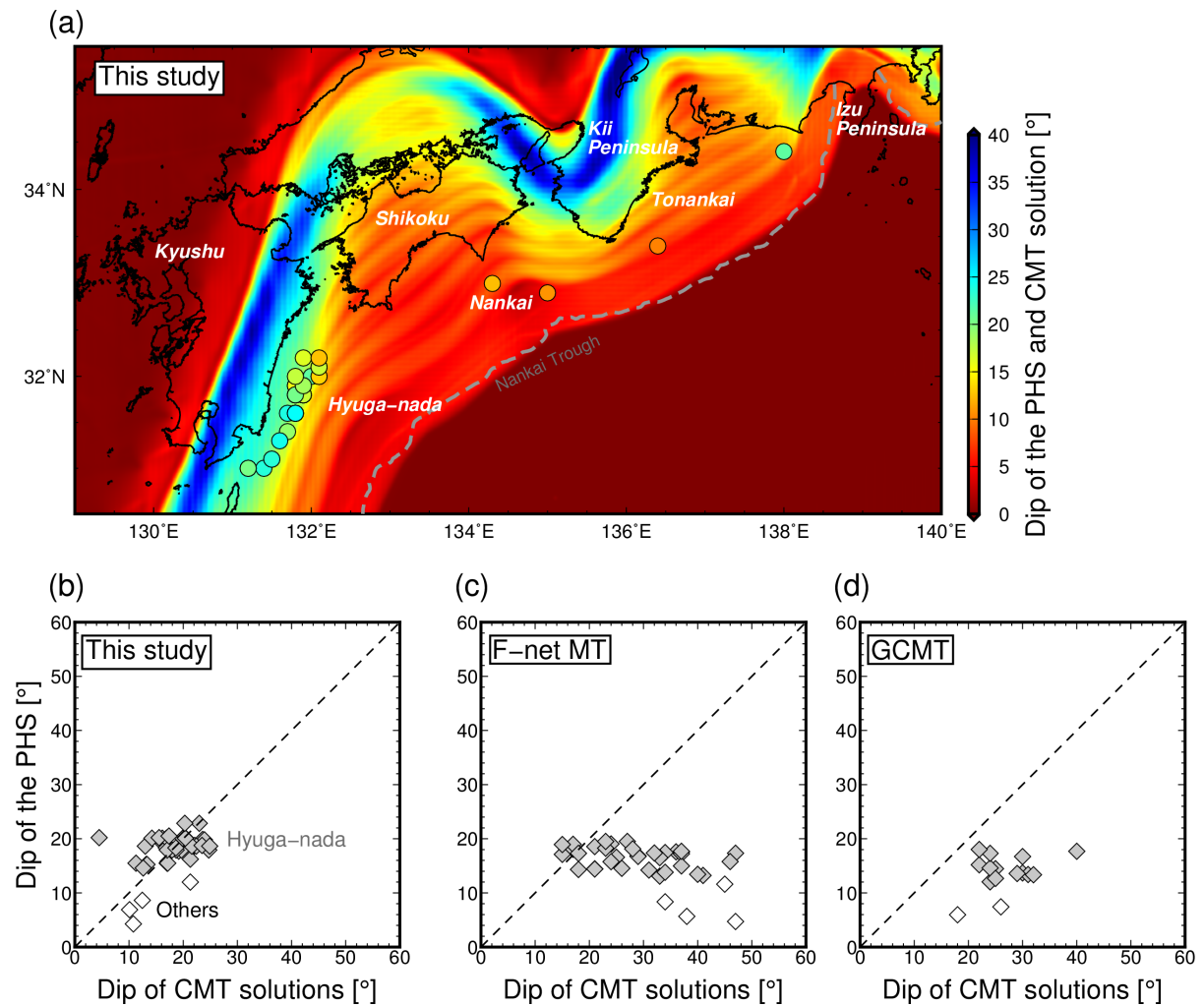
840



841

842 Figure 8. Spatial distributions of (a) correlation coefficients (CCs) of *P*-wave radiation
 843 patterns between 3D CMT and F-net solutions and (b) depth differences of 3D CMT
 844 solutions from the F-net catalogue. Lower right panels in (a) and (b) show histograms of
 845 CCs and differences, respectively. Offshore earthquakes are defined as earthquakes that
 846 occurred within regions closed by dotted lines in (a).

847



848

849 Figure 9. Comparisons of dip angles between the Philippine Sea plate (PHS) and CMT

850 solutions for suggestive interplate earthquakes. (a) Map of the region, comparisons of dip

851 angles of the Philippine Sea plate with (b) CMT solutions of this study and (c) F-net MT

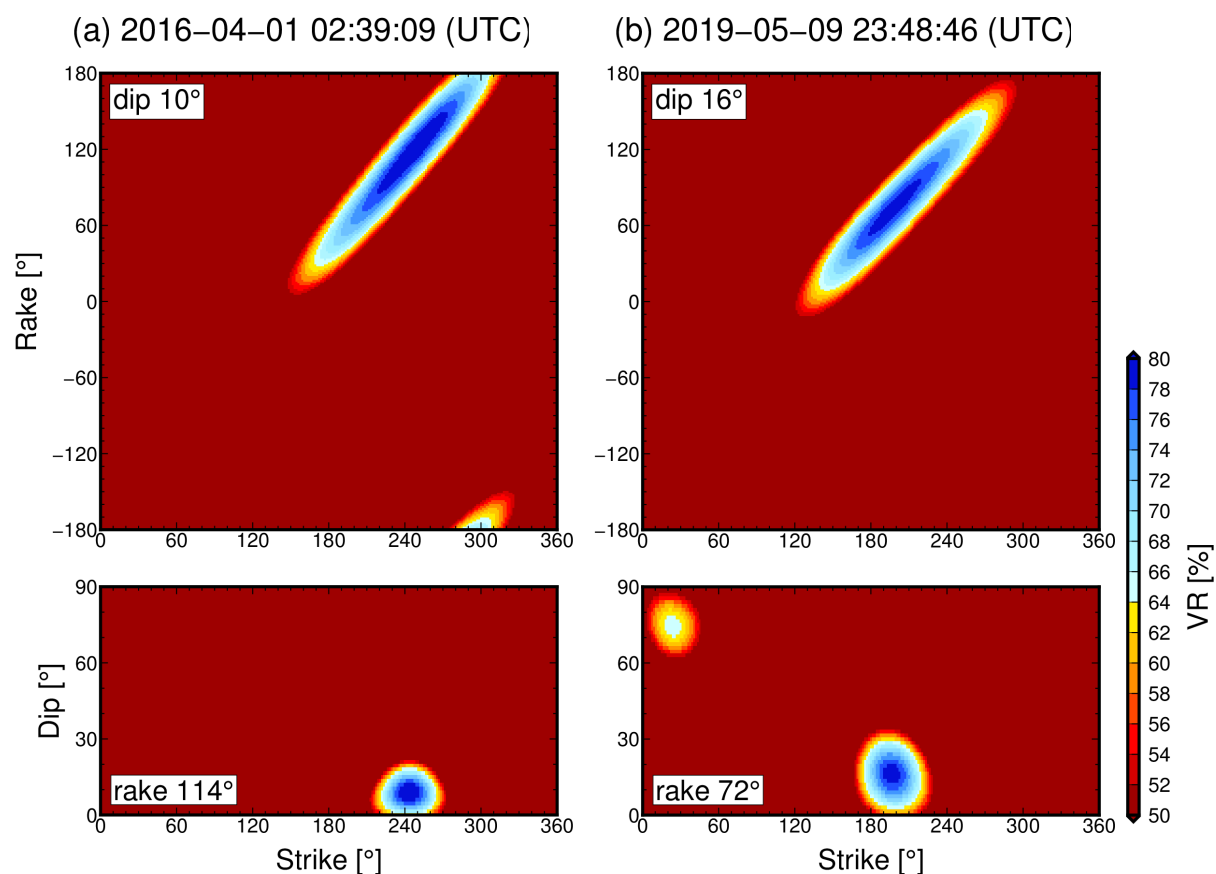
852 solutions. The background colour in (a) is representing spatial distribution of dip angles

853 of the Philippine Sea plate. The coloured circles denote dip angles of CMT solutions in

854 this study. We compared dip angles between the Philippine Sea plate and (c) F-net MT

855 and (d) GCMT solutions of corresponding earthquakes.

856



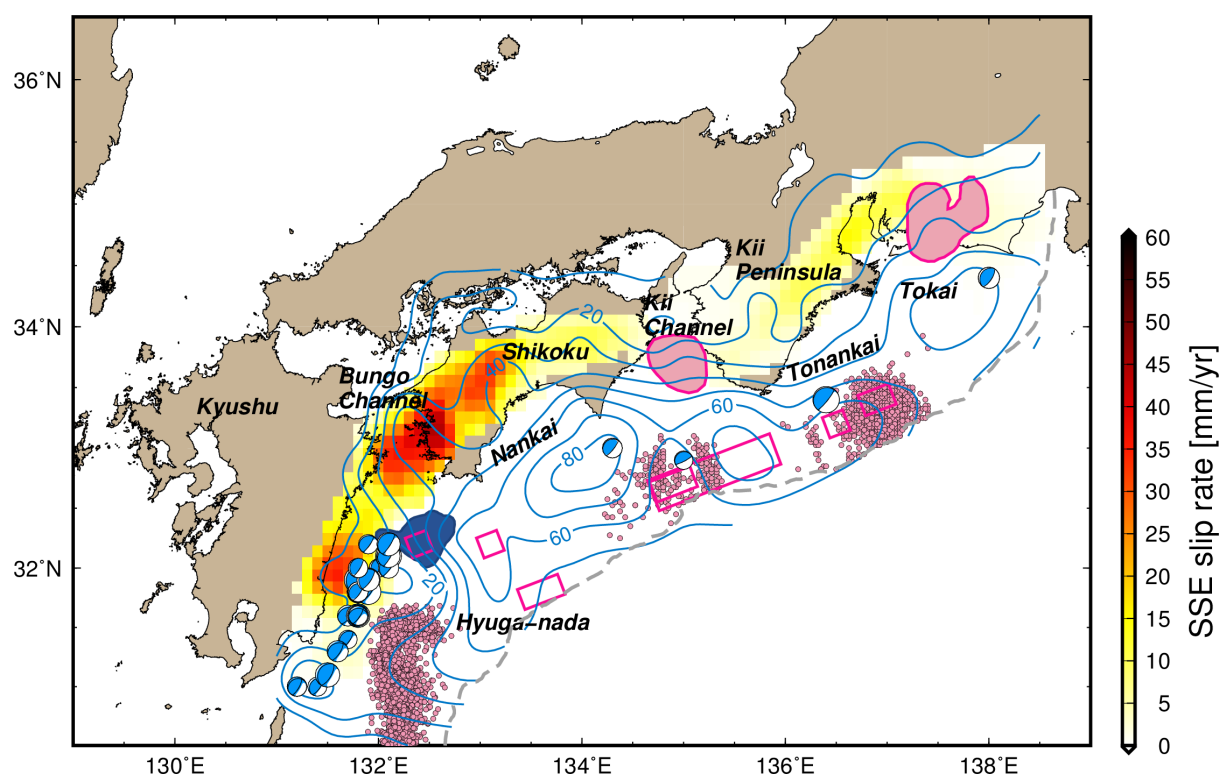
857

858 Figure 10. Distributions of variance reductions (VR) in the strike-rake and strike-dip planes
859 for (a) the southeast off Kii Peninsula earthquake on 1 April 2016 and (b) the Hyuga-
860 nada earthquake on 9 May 2019. In synthetics of displacement seismograms with various
861 strike, dip, and rake, we assumed pure double-couple point sources and fixed hypocenter
862 locations and seismic moments from CMT results (Figures 3 and 4).

863

864

865

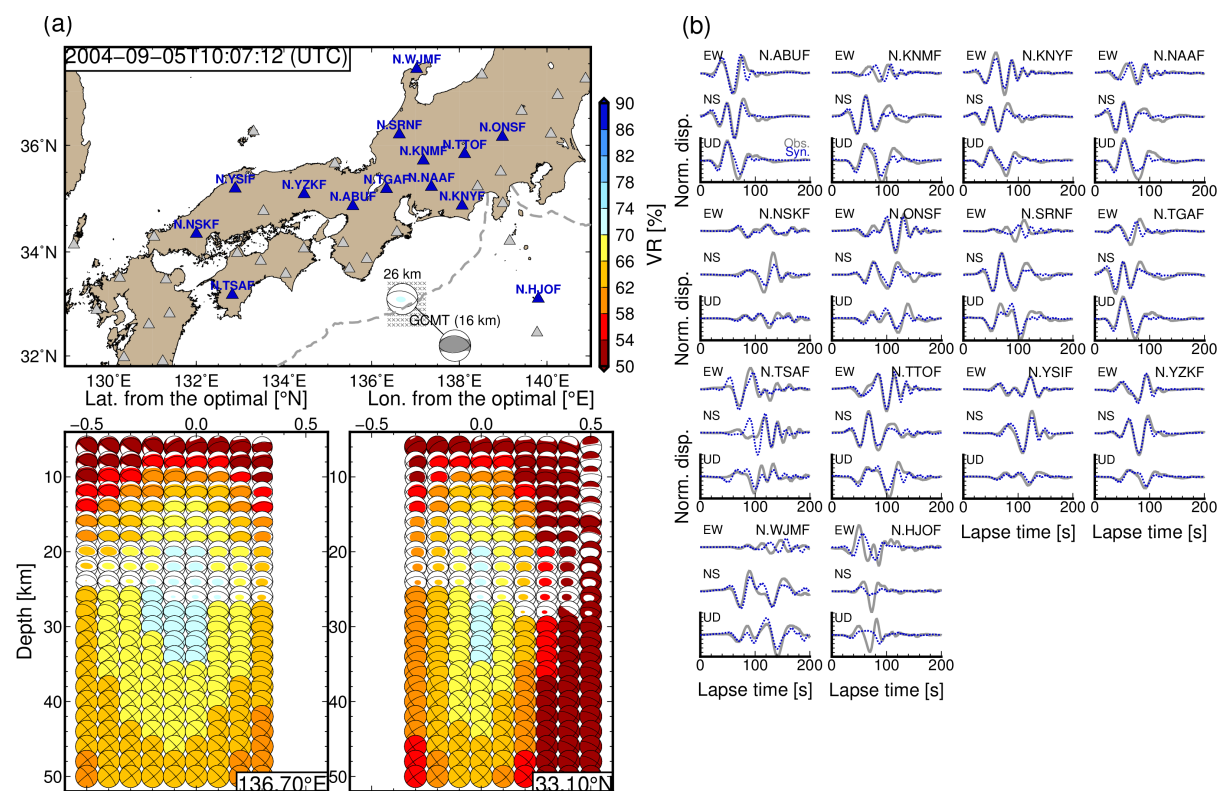


866

867 Figure 11. Spatial distribution of slip behaviours on the plate boundary along the Nankai
868 Trough. Plotted focal mechanisms are low-angle thrust faulting solutions at depths
869 around the plate boundary. The coseismic slip area of the 1968 M_w 7.5 Hyuga-nada
870 earthquake (Yagi *et al.* 1998) is shaded in dark blue. SSE slip rates were evaluated from
871 the combined SSE catalogues (Nishimura *et al.* 2013, Takagi *et al.* 2016, 2019). The pink
872 circles indicate the epicentres of the shallow LFTs of the Hyuga-nada and the shallow
873 VLFs in the Tonankai region referred from Yamashita *et al.* (2015) and Takemura,
874 Noda, *et al.* (2019). The pink shaded areas and pink rectangles indicate the large slip
875 areas of long-term SSEs (Kobayashi 2014, Miyazaki *et al.* 2006) and shallow SSEs
876 (Yokota & Ishikawa 2020), respectively. The blue contour lines indicate the slip-deficit
877 rates [mm/yr] on the plate boundary by Noda *et al.* (2018)

878

879

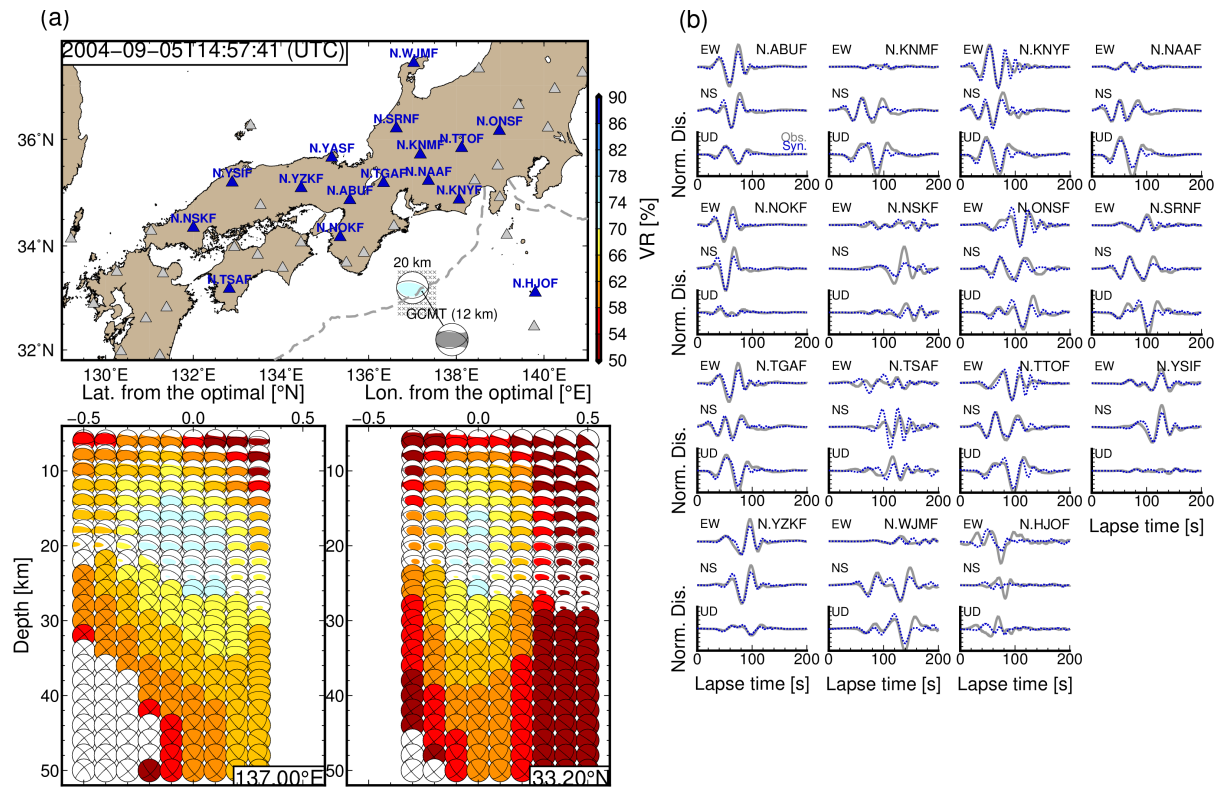


880

881 Figure 12. CMT results for the M_w 7.2 southeast off the Kii Peninsula earthquake that
 882 occurred on 5 September 2004. Grey focal mechanisms are the solutions of the F-net MT
 883 and GCMT catalogues. (a) Locations of the optimal solutions, used stations, and depth
 884 variations of optimal solutions at each source grid. Colours of the focal mechanisms
 885 reflect values of variance reduction between observed and synthetic displacements for
 886 25–100 s periods. The numbers above the optimal solutions in (a) are the optimal
 887 centroid depths. The grey focal mechanism in (a) is the F-net MT solution of this
 888 earthquake; (b) Comparisons of observed and synthetic displacements for 25–100 s
 889 periods. Grey solid and blue dotted lines are the observed and synthetic seismograms,
 890 respectively. Synthetic seismograms were evaluated by assuming the optimal solution.
 891 Amplitudes at each station were normalised by the maximum amplitude of both observed
 892 and synthetic three-component displacement waveforms. Detailed source parameters are
 893 listed in Table S2.

894

895



896

897

Figure 13. CMT results for the M_w 7.5 southeast off the Kii Peninsula earthquake that

898

occurred on 5 September 2004. (a) Locations of the optimal solutions, used stations, and

899

depth variations of optimal solutions at each source grid. Colours of the focal

900

mechanisms reflect values of variance reduction between observed and synthetic

901

displacements for 25–100 s periods. The numbers above the optimal solutions in (a) are

902

the optimal centroid depths. The grey focal mechanism in (a) is the F-net MT solution of

903

this earthquake; (b) Comparisons of observed and synthetic displacements for 25–100 s

904

periods. Grey solid and blue dotted lines are the observed and synthetic seismograms,

905

respectively. Synthetic seismograms were evaluated by assuming the optimal solution.

906

Amplitudes at each station were normalised by the maximum amplitude of both observed

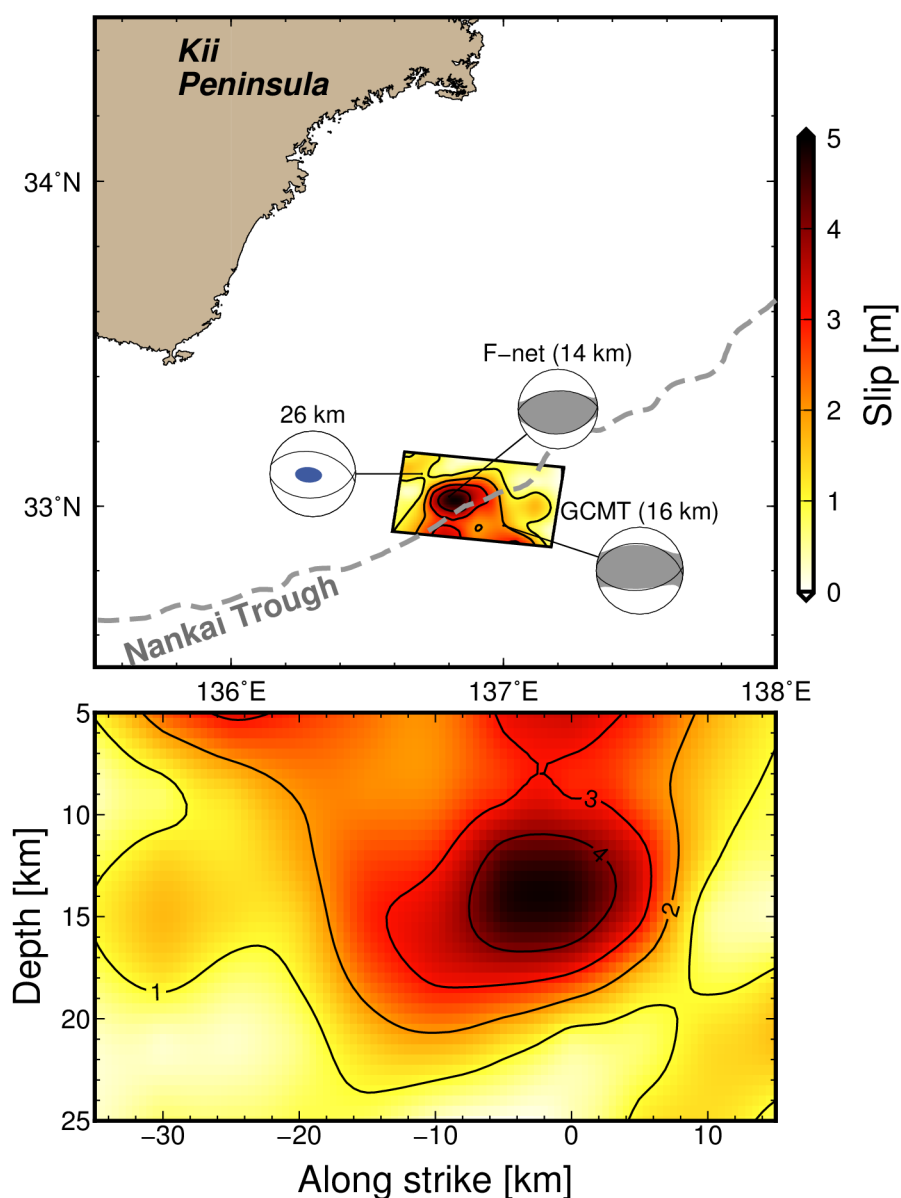
907

and synthetic three-component displacement waveforms. Detailed source parameters are

908

listed in Table S2.

909



910
911 Figure 14. Comparison of the CMT results for the M_w 7.2 southeast off the Kii Peninsula
912 earthquake and other CMT catalogues (Ekström *et al.* 2012, Fukuyama *et al.* 1998, Kubo
913 *et al.* 2002) and finite fault modelling (Okuwaki & Yagi 2018) solutions. The bottom
914 panel is the slip distribution of the finite fault model in the strike-depth plane.

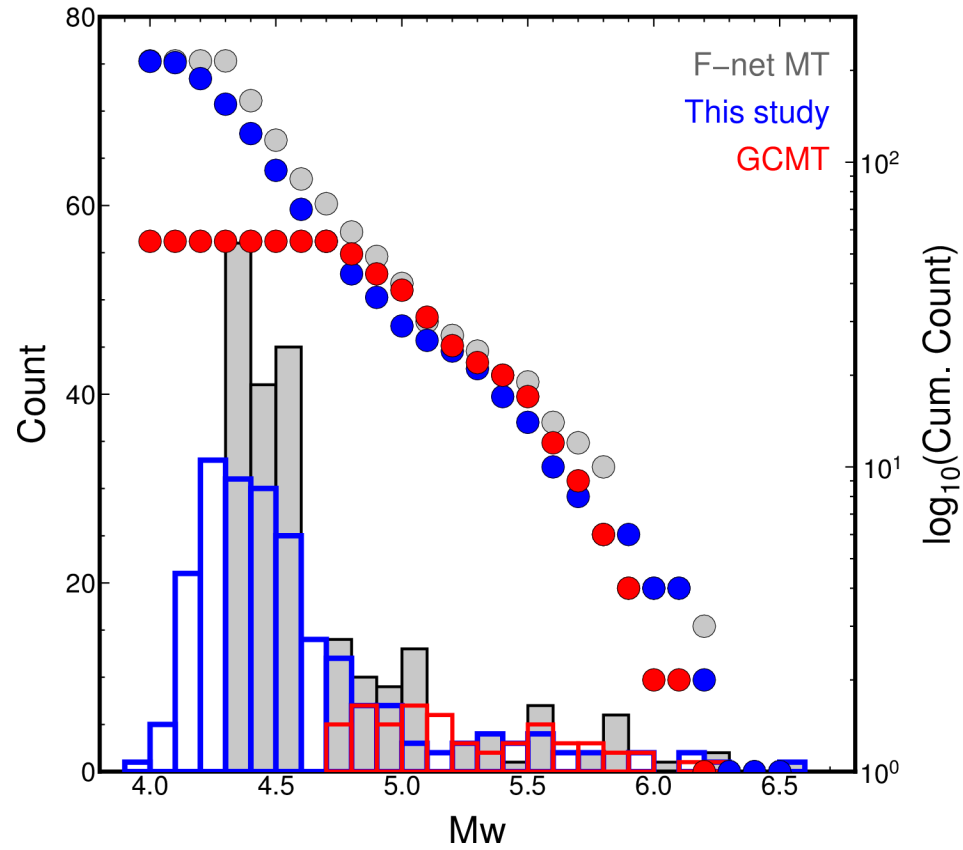


Figure S1. Size distribution of our 3D CMT catalogue (blue), the F-net catalogue (grey), and the GCMT catalogue (red). The selected criteria of the F-net and GCMT catalogue is same as in Figure 1.

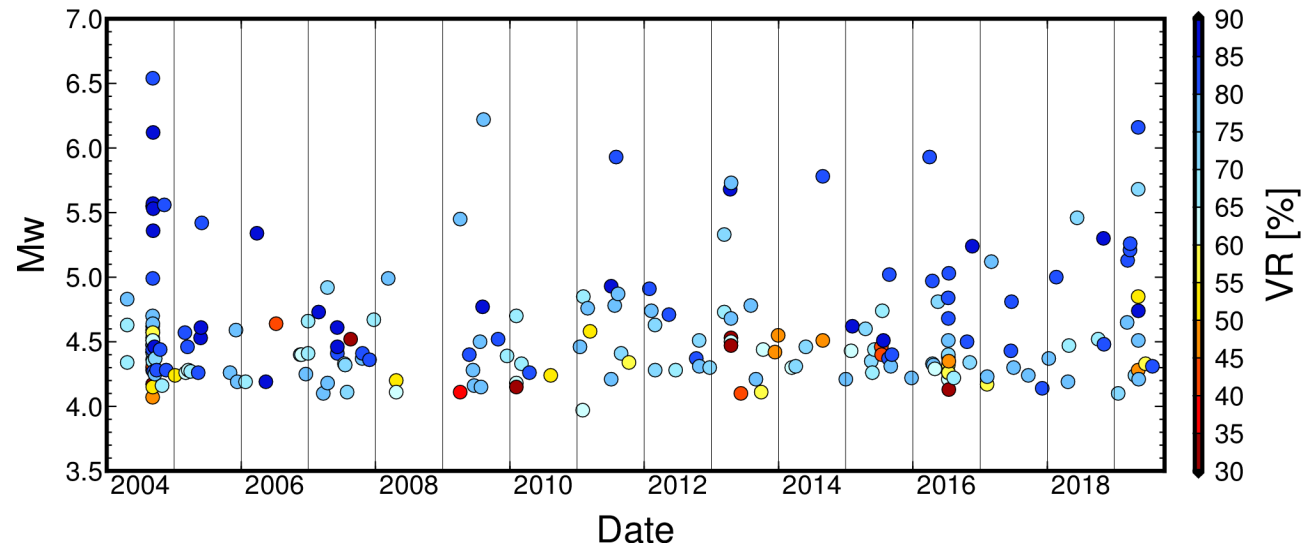


Figure S2. Magnitude-time diagram of our 3D CMT catalogue.

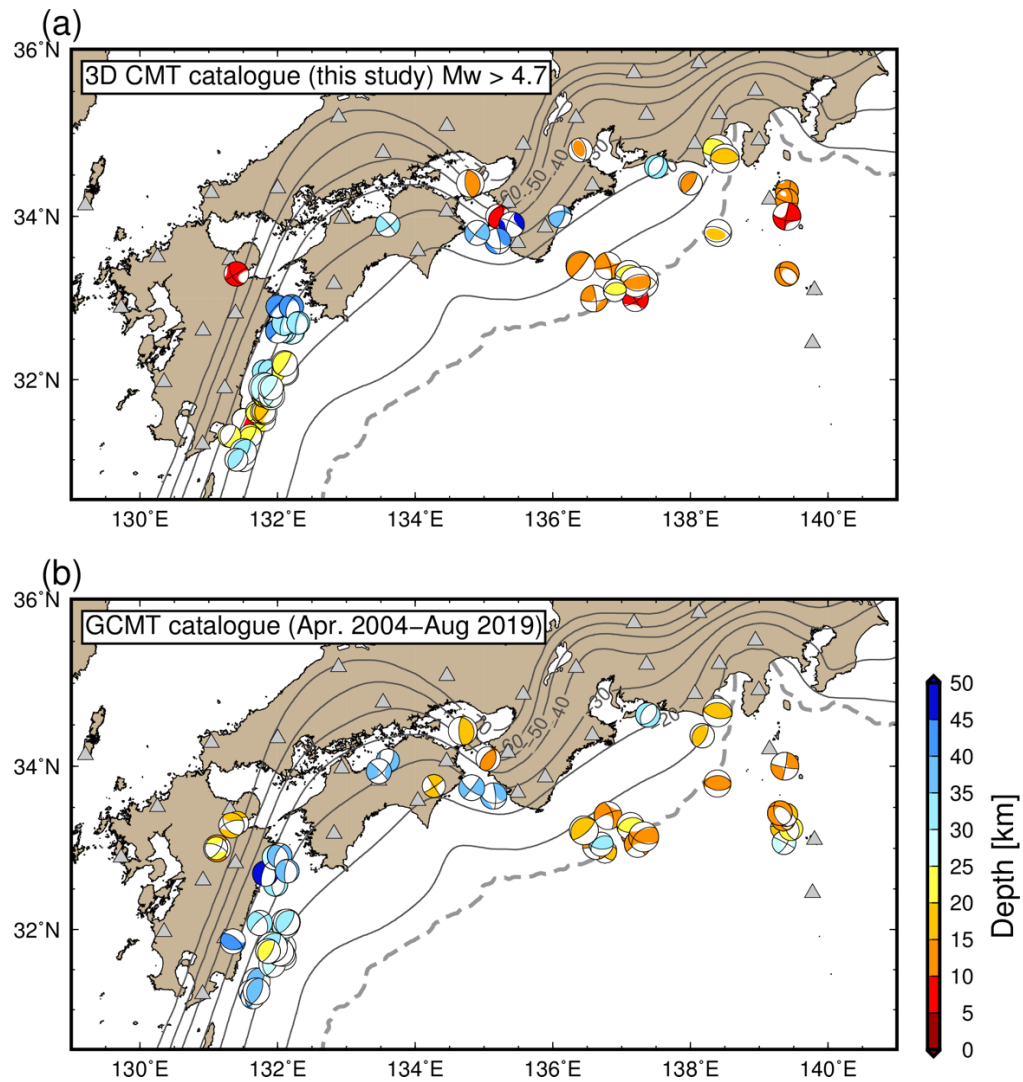


Figure S3. Similar as Figure 5 but for comparison with the GCMT catalogue. The M_w of plotted earthquakes in our 3D CMT catalogue is larger than 4.7, which is the lower limit of the GCMT catalogue (see Figure S1).

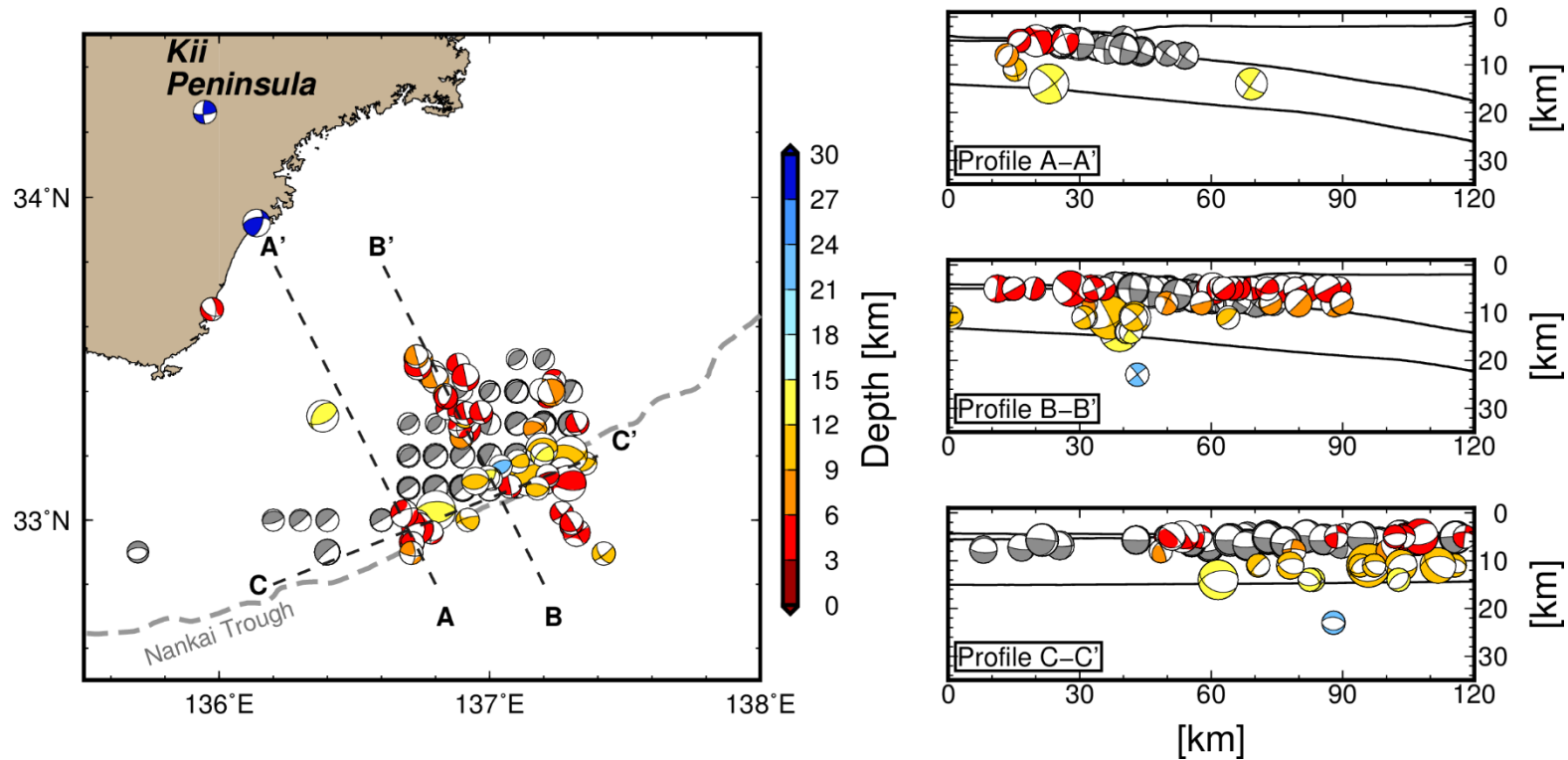


Figure S4. Spatial distribution of CMT solutions southeast of the Kii Peninsula. Coloured focal mechanisms are referenced from the F-net MT catalogue. Grey focal mechanisms are the CMT solutions of shallow VLFs (Takemura, Matsuzawa et al., 2019). Right-hand panels show cross-sections along profiles of A, B and C. The bathymetry of ETOPO1 (Amante & Eakins, 2009), the upper surface, and the oceanic Moho of the Philippine Sea Plate (Koketsu et al., 2012) along each profile are plotted in the right-hand panels.

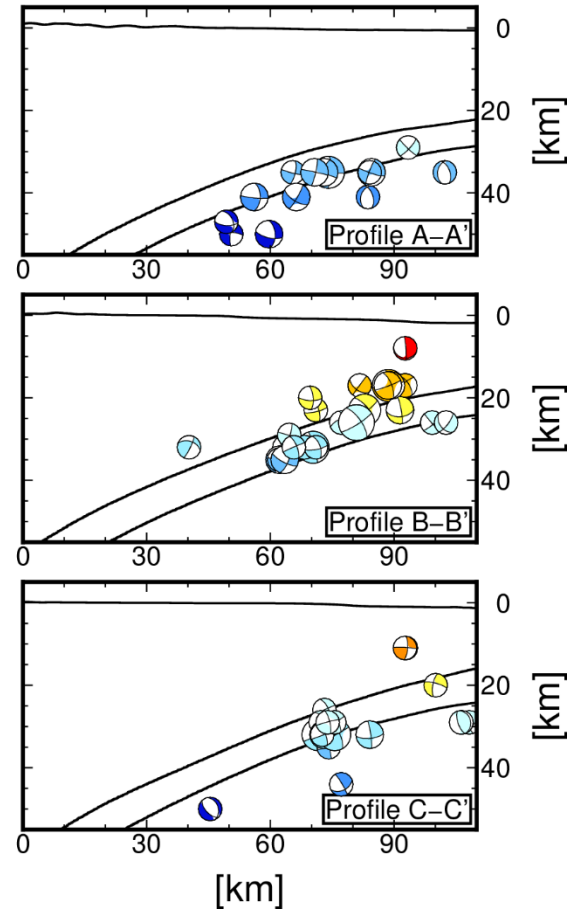
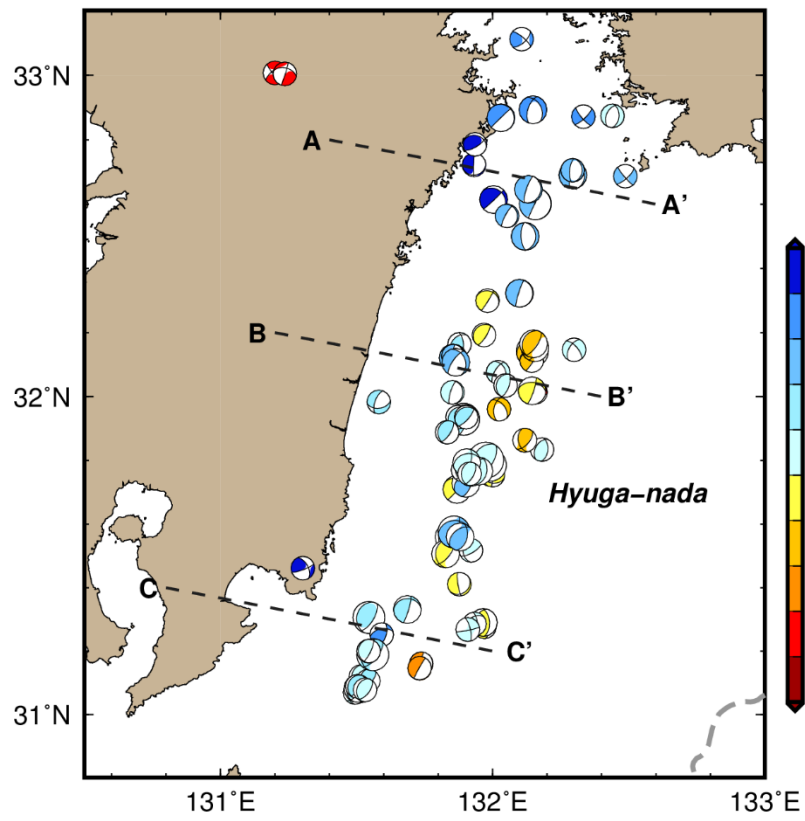


Figure S5. CMT results for the Hyuga-nada region.

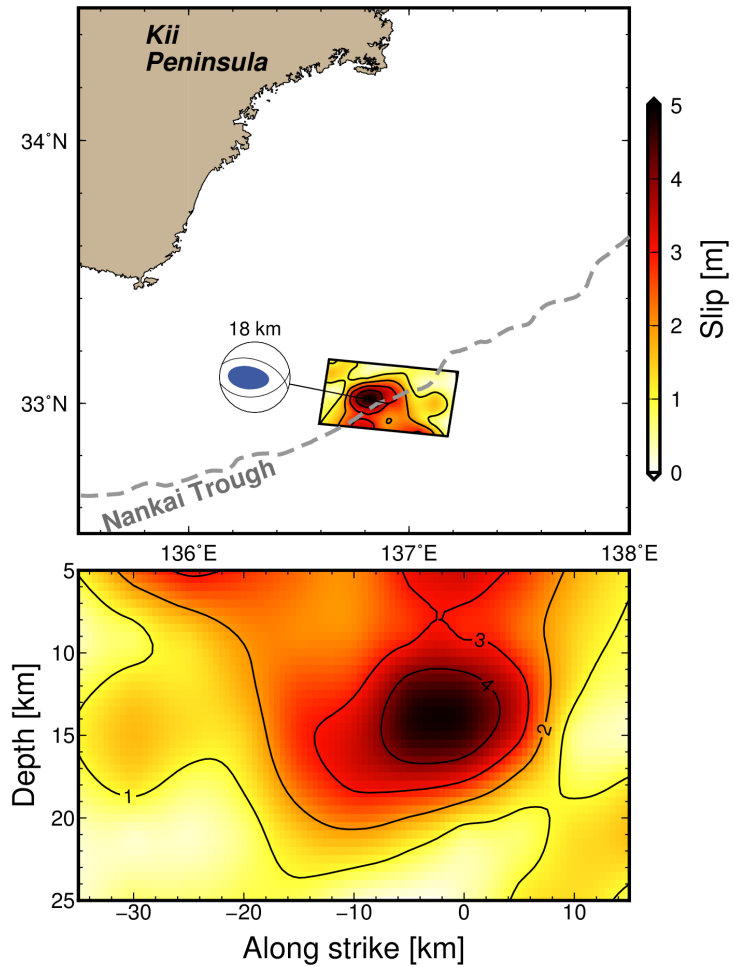


Figure S6. Comparison of the CMT results for the simulated M_w 7.2 southeast off the Kii Peninsula earthquake using the finite fault modelling (Okuwaki & Yagi 2018) solutions. In this CMT inversion, simulated seismograms using the finite fault modelling (Okuwaki & Yagi 2018) solution were used as observed seismograms. The bottom panel is the slip distribution of the finite fault model in the strike-depth plane.

Table S1. CMT solutions for all analysed moderate earthquakes.

Centroid time (UTC)	Lon.	Lat.	Depth [km]	M_{rr}	$M_{\theta\theta}$	$M_{\phi\phi}$	$M_{r\theta}$	$M_{r\phi}$	$M_{\theta\phi}$	Exp.	Mw	VR [%]
2004-04-21T07:26:30	132.3	33.5	38	-1.5100	-1.8500	2.9000	-2.4800	-1.2300	1.3700	22	4.34	67.45
2004-04-21T21:10:41	131.8	31.6	20	0.9760	0.2520	-0.3590	0.5200	0.6680	-0.2540	23	4.64	68.22
2004-04-21T21:20:52	131.8	31.5	24	1.9100	0.5570	-1.1000	0.7080	1.1300	-0.8800	23	4.84	78.46
2004-09-06T14:31:02	136.8	33.4	12	0.6040	-0.8920	1.5300	0.5790	0.5210	2.1800	24	5.55	82.86
2004-09-06T16:48:42	137.1	33.1	20	8.9900	-7.9500	0.5620	-0.1920	-2.1800	-2.2800	22	4.57	35.87
2004-09-06T17:59:37	136.9	33.5	14	0.0678	-0.5330	0.4660	0.0528	0.2790	0.9020	23	4.62	71.96
2004-09-06T20:06:48	137.1	33.6	8	1.5300	3.1600	-1.0500	2.1700	1.7800	-0.2500	22	4.32	65.56
2004-09-06T20:45:39	137.2	33.0	10	-0.3520	-2.4200	1.0300	-1.0300	-0.1840	1.0200	22	4.18	34.71
2004-09-06T22:49:05	136.8	33.4	14	-0.1690	-0.7280	0.9130	-0.4740	0.9630	0.8910	22	4.07	46.53
2004-09-06T22:59:28	136.8	33.5	12	0.5830	-2.8800	4.0400	-0.5310	1.2600	3.9300	22	4.42	77.34
2004-09-06T23:28:52	136.8	33.5	14	0.9900	-2.3300	3.3500	-1.0300	1.7300	2.6700	22	4.37	61.55
2004-09-07T00:35:45	137.0	33.1	8	0.7790	-2.0700	2.3900	-0.3200	3.3300	3.4900	22	4.42	66.03
2004-09-07T00:46:48	136.8	33.5	14	1.3300	-3.6700	5.5700	-1.6400	3.1700	4.4600	22	4.52	74.39
2004-09-07T00:54:35	136.7	33.5	16	-0.1140	-7.2000	6.7400	-1.2300	2.3000	6.3300	22	4.59	80.49
2004-09-07T01:10:05	136.8	33.4	14	0.5490	-3.1200	3.9500	-2.0500	3.9300	3.2200	22	4.48	77.42
2004-09-07T02:20:32	137.3	33.2	24	5.9200	-6.1500	0.2230	-1.5100	0.6320	-1.4300	22	4.47	76.12
2004-09-07T03:11:57	136.9	33.0	16	0.8740	-0.9970	0.2930	-0.7250	-0.0274	0.7540	23	4.70	78.61
2004-09-07T04:29:18	137.1	33.2	24	4.9000	-10.1000	0.6640	1.9100	-0.0017	-0.7360	22	4.54	68.2
2004-09-07T04:39:47	137.2	33.1	12	0.8410	-6.4300	2.4600	-0.1140	3.1000	0.3390	22	4.44	81.55
2004-09-07T04:59:32	136.6	32.9	8	0.7040	-1.2800	1.3200	1.2200	-0.9690	2.5300	22	4.28	59.12
2004-09-07T10:45:29	136.7	33.5	14	-0.0107	-0.7450	0.9020	-0.1830	0.3450	0.6880	23	4.64	78.17

2004-09-07T11:23:37	136.7	32.9	6	0.8930	0.5190	0.5580	4.0400	7.3800	3.1600	22	4.57	56.97
2004-09-07T14:02:48	136.7	33.5	16	-0.0584	-0.6920	0.8610	-0.2420	0.1940	1.2300	22	4.05	59.38
2004-09-07T17:29:41	137.3	33.2	24	4.3300	-11.2000	-0.4320	-1.4100	1.4000	-0.0673	25	6.56	81.44
2004-09-08T00:10:04	137.2	33.2	16	2.3000	-3.5800	-1.0400	-2.2200	-0.1920	-0.9520	23	5.00	82.86
2004-09-08T00:17:50	137.1	33.7	10	1.1100	2.1200	-1.0100	0.9700	0.8070	0.5910	22	4.17	51.85
2004-09-08T04:58:53	137.2	33.3	10	0.9130	-2.9700	5.0100	-0.3630	4.9100	3.5000	22	4.51	63.08
2004-09-08T05:56:30	137.0	33.4	12	-0.2580	-0.0829	3.1500	-1.0700	-2.4800	1.6200	22	4.32	42.47
2004-09-08T11:20:24	136.9	32.7	6	0.3250	-2.3400	2.6100	-1.2600	-2.5700	1.8700	22	4.35	67.83
2004-09-08T12:36:23	137.1	33.3	22	2.3700	-2.9700	-0.1930	0.9000	-0.2030	-0.1730	24	5.57	85.05
2004-09-08T15:02:14	137.1	33.6	8	1.2300	1.2300	-0.2840	1.6900	0.7740	0.0002	22	4.17	57.56
2004-09-09T08:40:10	137.2	33.0	8	0.1450	-1.4000	0.9040	-0.4990	0.2190	0.5310	24	5.36	85.86
2004-09-09T08:58:27	137.2	33.2	12	1.1200	-2.3800	0.2500	-0.3270	-0.3450	-0.2470	25	6.13	89.29
2004-09-10T20:05:57	136.6	33.0	10	0.0795	-0.4280	0.5350	0.4930	0.9040	2.1700	24	5.53	86.87
2004-09-12T03:05:58	136.7	32.9	10	0.2740	-1.3400	1.6600	-0.5860	2.0400	1.9200	22	4.27	83.36
2004-09-17T12:56:28	136.6	32.9	10	-0.5720	-0.4840	1.1900	2.8500	3.2900	4.2700	22	4.46	87.03
2004-09-18T18:48:38	136.8	33.5	12	0.1220	-0.6940	1.9900	0.1600	0.4740	2.5600	22	4.25	77.3
2004-09-20T14:17:51	137.2	33.6	8	0.4310	2.9600	-4.2100	2.2000	-0.4970	-1.3700	22	4.37	74.09
2004-09-28T09:37:43	137.3	33.0	10	0.4440	-1.9900	1.1600	-2.1800	1.1900	1.3100	22	4.28	83
2004-10-03T17:00:20	136.8	33.4	12	-0.2920	0.5230	3.2200	0.4630	0.2370	0.1240	22	4.18	71.88
2004-10-17T16:05:41	137.2	33.2	22	3.7600	-5.3300	1.0000	-1.2900	-2.6500	-1.9000	22	4.44	82.04
2004-10-28T06:27:30	135.2	33.6	34	-0.3740	-1.6700	2.2300	0.0469	-0.4460	-0.8680	22	4.16	69.66
2004-11-09T09:07:27	138.4	33.8	16	1.2800	-3.5400	-0.4050	-1.0100	0.6480	0.3660	24	5.58	82.93
2004-11-19T14:46:27	137.1	33.2	12	1.5700	-4.6800	-0.8920	-0.7280	-0.4220	-0.4780	22	4.31	80.91
2005-01-06T08:49:12	139.3	34.2	8	2.6600	-1.8000	3.3200	0.0929	0.5320	0.6500	22	4.29	53.42

2005-03-01T15:59:45	136.9	33.4	12	3.8000	-3.0200	7.6100	3.1300	1.8900	6.0700	22	4.59	84.06
2005-03-05T23:58:49	131.2	31.4	42	1.2400	-1.6700	1.4600	0.8400	1.2300	2.0300	22	4.26	64.99
2005-03-15T04:49:31	137.0	33.1	28	5.8700	-4.6000	-0.8160	-2.4000	-0.0550	-2.0400	22	4.46	82.27
2005-03-19T20:34:09	137.2	33.0	24	2.4000	-4.1300	0.0492	-0.3670	0.0348	-0.3640	22	4.29	64.7
2005-04-01T18:41:48	131.4	31.0	32	3.0500	-0.1300	-0.8730	1.1700	1.8200	-1.0400	22	4.28	68.09
2005-05-12T13:22:50	132.0	32.1	28	-0.6250	-0.0351	3.6100	1.3700	1.5400	0.5930	22	4.28	82.71
2005-05-26T05:31:29	132.3	33.4	46	-3.2300	-4.4200	7.2800	3.3400	2.2300	-1.7300	22	4.53	85.27
2005-05-27T12:17:18	133.7	34.0	36	-0.3810	-0.4810	1.0700	-0.4680	-0.3470	0.0844	23	4.61	89.65
2005-05-31T20:04:14	131.5	31.3	30	1.6900	0.7830	-0.3400	0.9510	0.8890	-0.3210	24	5.45	81
2005-11-01T21:47:34	135.1	33.8	46	-0.9580	0.6550	0.6100	-2.2700	-1.4100	1.1500	22	4.26	78.44
2005-12-03T19:39:01	137.0	33.1	26	8.7900	-8.7000	-4.0800	0.1430	0.8020	-3.3100	22	4.59	77.63
2005-12-03T20:01:21	137.0	33.1	28	4.3900	-7.3300	-4.8500	1.1900	1.4600	-4.1800	22	4.55	73.32
2005-12-11T03:32:08	132.0	32.0	26	1.5500	0.0063	-1.2300	1.2500	1.4500	-0.4200	22	4.19	76.16
2006-01-25T06:36:46	131.7	31.4	20	1.9700	-0.0443	-0.3050	1.0000	1.6100	-0.7570	22	4.20	67.21
2006-03-27T20:50:25	132.2	32.6	34	0.5430	0.3400	0.7660	0.6620	1.1100	-0.0280	24	5.38	86.62
2006-05-15T10:42:10	135.2	34.2	6	0.7870	0.3760	-3.2700	-0.0809	0.6340	-0.7800	22	4.21	86.19
2006-07-10T02:48:05	139.4	34.3	14	1.2700	0.2770	1.6400	-0.0862	0.1950	-0.8850	23	4.76	40.87
2006-11-18T10:08:35	132.0	31.9	32	-1.9100	-1.7900	5.5000	2.4100	-0.5070	-1.1900	22	4.41	75.13
2006-11-26T00:39:44	132.1	32.0	10	4.2400	0.7990	0.0740	2.6200	3.5400	-0.3240	22	4.42	60.13
2006-11-25T12:28:49	131.6	32.0	42	-0.3890	2.3300	0.9110	-0.1350	1.8300	1.9100	22	4.27	79.22
2006-11-25T11:49:31	139.4	34.2	12	0.4630	0.9330	1.4500	-0.6150	0.1020	-0.9650	23	4.75	67.16
2006-11-25T12:42:10	139.3	34.2	12	-1.7800	4.1300	2.8200	1.4000	-0.4390	-3.8400	22	4.43	69
2007-02-26T05:41:21	136.9	33.1	22	1.4000	-1.4700	-0.0424	0.6020	-0.2340	-0.1850	23	4.73	85.6
2007-03-24T01:20:52	136.9	33.4	10	0.2360	-0.7510	1.2100	0.2090	0.6620	1.3500	22	4.11	76.6

2007-04-15T21:19:28	136.4	34.8	14	1.9000	-1.1000	-3.3000	0.5050	0.7610	1.2400	23	4.94	71.68
2007-04-16T03:34:44	136.4	34.8	12	1.6900	0.0968	-2.4300	0.8840	-0.5490	0.1330	22	4.18	77.15
2007-04-26T18:02:54	133.6	33.9	34	0.5410	-3.3800	3.2000	-0.3530	0.9470	0.6560	23	4.96	88.57
2007-06-07T08:42:48	131.5	33.3	10	0.1110	1.2900	-0.4550	0.0837	0.3930	-0.2780	23	4.62	87.28
2007-06-08T02:22:14	131.5	33.3	8	0.6900	7.2800	-1.1500	0.3940	2.2100	-1.7100	22	4.45	84.5
2007-06-08T05:50:38	131.5	33.3	8	-0.3410	7.7300	-1.9500	-0.8060	2.8100	-1.6300	22	4.48	85.79
2007-07-17T02:24:17	135.9	34.3	38	0.1960	0.6830	0.2060	0.1410	-0.7580	-3.9000	22	4.34	61.32
2007-07-21T02:15:24	139.4	34.8	12	1.9700	0.9580	-0.2440	-1.0400	-1.0800	-3.2600	22	4.33	71.52
2007-07-31T19:22:39	131.9	32.2	26	1.9500	0.6120	-1.1400	-0.2330	0.8090	-0.4540	22	4.12	70.23
2007-08-19T19:21:54	138.6	34.0	50	0.5570	3.9900	-0.2680	3.3500	-6.0000	-2.0200	22	4.52	31.48
2007-10-21T11:09:26	131.9	32.2	28	2.3700	-0.8360	-0.5320	2.1100	3.3000	-1.3300	22	4.37	76.79
2007-10-22T18:35:59	139.1	34.2	14	6.5700	-0.7260	6.6900	-1.5000	2.5700	0.6990	22	4.51	83.03
2007-11-30T05:17:47	131.9	32.7	44	0.8450	-0.0984	2.3800	0.5950	4.0000	1.1800	22	4.37	83.26
2007-12-23T11:49:05	131.6	31.2	26	0.7680	-0.0350	0.6130	0.2310	1.0000	-0.6550	23	4.70	69.39
2008-03-10T19:44:30	131.8	31.8	18	3.1300	0.0972	-0.2790	1.7700	2.7100	-0.8190	23	5.00	75.47
2008-04-23T03:07:19	131.4	31.0	28	0.3990	-1.4000	-0.4010	-1.2200	-1.0600	-1.7300	22	4.21	54.25
2008-04-23T03:26:10	131.5	31.0	24	1.0200	-0.4460	0.8440	-1.0300	-0.8560	-0.9920	22	4.13	62.9
2009-04-06T03:36:27	131.9	31.9	26	1.6000	0.3630	-0.2710	0.9720	1.2800	-0.3600	24	5.47	78.17
2009-04-06T03:53:17	131.8	31.9	28	1.3600	0.3350	0.5540	0.9970	1.3700	0.4610	22	4.14	37.31
2009-05-26T05:26:20	137.8	34.7	28	0.4350	-4.6400	4.5700	-0.1080	1.6200	0.7650	22	4.40	82.58
2009-06-15T04:17:53	132.1	33.1	50	1.0400	-1.9200	3.5000	-0.3130	1.8300	0.0194	22	4.29	78.16
2009-06-20T13:22:17	135.0	32.9	6	0.9780	-0.4630	-0.0802	1.8300	0.9460	-0.3280	22	4.16	76.56
2009-07-23T08:51:00	134.3	33.0	16	2.0000	-2.1600	-1.5300	3.9200	5.1600	-1.5800	22	4.50	77.36
2009-07-28T14:30:54	131.8	32.0	32	0.3260	1.3800	2.5300	0.8300	1.4600	0.5420	22	4.22	77.51

2009-08-05T21:51:13	132.1	32.6	34	-0.6180	0.4690	2.1400	0.0996	1.1400	0.0227	23	4.80	85.05
2009-08-11T14:07:08	138.4	34.8	22	2.3400	-1.9500	0.5600	1.0700	0.7670	0.9580	25	6.22	79.55
2009-10-29T11:37:08	132.0	32.4	32	0.3630	4.3700	8.6200	2.2600	5.8200	0.9270	22	4.58	80.96
2009-12-16T23:12:50	133.4	33.2	30	0.7220	-3.7400	4.2200	-2.6800	-0.1910	-0.0985	22	4.39	69.81
2010-02-05T02:41:58	131.5	31.5	10	-2.2300	-0.2730	-0.3570	-0.9350	-1.8500	0.0247	22	4.21	61.72
2010-02-05T05:30:08	131.5	31.5	8	-0.7890	-0.1860	-0.3460	-0.5180	-1.2800	0.0114	23	4.72	65.27
2010-02-05T05:35:21	131.5	31.1	28	-0.5990	-0.2270	-1.4200	-0.5510	-1.7100	-0.9070	22	4.17	33.1
2010-03-05T15:49:55	139.5	33.8	16	-0.1790	-2.5100	3.7300	0.6980	-0.0789	-2.2300	22	4.33	69.12
2010-04-17T14:34:55	132.5	33.6	40	-2.3500	0.7910	2.2700	1.3300	-0.9060	-1.1100	22	4.26	84.9
2010-04-18T06:24:06	132.4	32.9	32	-2.1800	0.6880	3.2000	0.4310	-0.2830	0.8580	22	4.25	51.64
2011-01-17T05:33:22	133.8	34.0	36	-0.1260	-3.5100	3.7600	-0.6940	0.9810	4.8400	22	4.46	78.87
2011-02-01T11:32:24	132.0	31.7	22	0.8540	-0.3790	-0.5040	0.2120	0.5490	-0.6000	22	3.97	62.9
2011-02-05T03:11:23	131.5	31.0	32	2.7500	0.1790	-1.0300	0.9620	0.8370	-0.6420	23	4.87	68.85
2011-02-28T18:04:33	131.8	32.1	34	-0.4780	0.4270	2.0200	0.7020	0.9010	0.3580	23	4.79	78.53
2011-03-13T07:11:01	136.8	33.0	10	0.5130	-0.8780	6.0500	3.2200	1.0900	8.0300	22	4.59	52.28
2011-07-06T04:18:41	135.2	34.0	8	2.8800	-0.1930	-1.9900	-0.0750	1.2100	-1.4300	23	4.93	86.46
2011-07-06T04:34:53	135.2	34.0	8	2.2300	-0.3010	-1.8600	0.1840	1.1000	-1.1500	22	4.21	75.28
2011-07-25T08:32:11	136.1	34.0	38	1.2500	-0.6200	-0.0724	-0.4360	0.8300	-1.3200	23	4.79	78.51
2011-08-02T08:58:12	138.5	34.7	18	8.7200	-8.3200	-0.4010	4.6400	0.4010	0.2340	24	5.93	81.6
2011-08-12T13:37:45	138	34.4	10	1.7300	-0.5450	-1.1900	1.0100	1.5400	-0.7180	23	4.87	76.42
2011-08-28T18:52:02	131.2	31.0	30	5.5100	-0.3220	0.3930	1.8000	3.4000	-1.3800	22	4.44	70.95
2011-10-11T04:19:27	134.1	34.0	38	-1.8000	-0.9610	3.3900	-2.5100	1.3900	-0.4370	22	4.34	55.4
2012-01-30T12:18:20	132.0	32.6	44	0.6040	-0.4710	1.1500	2.0800	1.8100	-0.2870	23	4.91	84.49
2012-02-09T21:55:14	131.6	31.3	24	1.5200	-0.1100	0.0839	0.5160	1.1200	-0.6240	23	4.76	77.61

2012-02-29T10:23:01	131.9	31.8	18	0.9930	0.2130	-0.2410	0.5610	0.6860	-0.2020	23	4.65	70.72
2012-03-01T04:33:32	131.8	31.6	18	1.6200	0.6990	-0.7530	1.1600	2.8400	0.0018	22	4.28	72.98
2012-05-14T21:36:43	131.7	31.6	24	1.2300	-0.2870	0.0972	0.5740	0.9540	-0.5520	23	4.72	82.78
2012-06-20T12:35:32	132.3	32.1	30	-1.6900	-1.1000	3.3300	1.7200	-0.7720	-0.2970	22	4.28	68.9
2012-10-10T14:49:33	132.5	32.7	26	-0.1940	-4.5100	4.0800	-0.5900	0.4700	0.8570	22	4.37	80.93
2012-10-26T10:54:13	131.9	31.9	28	6.9100	-0.5030	-2.2800	3.7600	3.0000	-2.4500	22	4.52	74.92
2012-10-27T13:44:35	133.5	33.5	32	0.2950	-2.8700	3.2900	2.0400	-0.4650	-0.1490	22	4.32	78.78
2012-12-23T00:15:28	132.3	33.6	44	-2.2800	1.1800	3.8100	0.0741	1.6400	-0.4460	22	4.31	74.72
2013-03-12T03:34:51	131.8	31.6	22	1.0500	0.2970	-0.4430	0.5970	0.7460	-0.2560	24	5.34	74.59
2013-03-12T03:59:44	131.8	31.6	18	1.5200	0.3480	-0.3950	0.8020	0.9360	-0.2940	23	4.75	68.12
2013-04-13T14:33:17	134.8	34.4	14	3.2300	-0.0934	-4.0200	0.1170	-1.9900	0.7870	24	5.68	86.62
2013-04-17T19:15:22	139.4	34.1	12	3.3400	0.5930	-5.9100	-3.6200	0.7030	-4.9700	22	4.53	26.36
2013-04-17T20:13:57	139.5	34.0	6	2.5100	4.8900	-1.6900	1.3000	-0.0078	-6.0300	22	4.51	62.63
2013-04-17T20:16:18	139.4	34.1	10	-1.5600	3.7900	-2.3900	-1.1400	-1.6500	-4.9700	22	4.47	32.05
2013-04-17T21:22:12	139.4	34.1	10	0.0273	0.8930	-0.6150	-0.3640	-0.2790	-0.9960	23	4.68	75.46
2013-04-18T02:57:36	139.4	34.0	8	0.9590	-1.0200	2.1000	-0.2260	-2.0000	-4.3200	24	5.74	78.29
2013-06-10T19:11:01	139.4	33.2	10	1.8000	0.4650	1.0300	-1.5100	0.7290	0.1010	22	4.17	41.52
2013-08-03T18:56:13	137.5	34.6	32	-1.4300	0.9170	1.7500	-0.2710	-0.2480	0.7870	23	4.79	78.63
2013-08-18T17:00:59	139.4	33.3	12	0.1380	0.1800	0.4230	-0.1540	0.4480	-1.2100	23	4.69	74.86
2013-08-31T02:32:24	135.9	33.7	8	-1.4700	0.3350	2.0900	-0.1970	-0.5020	-1.8300	22	4.21	76.14
2013-09-28T13:37:47	131.5	31.2	28	1.7700	-0.7440	0.0424	0.1470	1.0500	-0.7720	22	4.12	58.21
2013-10-09T05:45:21	131.9	31.8	20	4.5900	0.5480	-1.4400	3.0400	3.6200	-1.4600	22	4.45	62.64
2013-12-12T20:25:13	131.2	31.2	30	-2.0100	0.9670	2.8600	-2.6700	-3.8600	-0.0001	22	4.42	48.1
2013-12-29T19:17:49	139.5	33.3	50	-0.8930	1.2000	3.9800	-3.3700	1.6700	-6.9600	22	4.55	48.6

2014-03-13T16:35:53	131.4	31.0	26	4.0700	0.1290	-1.5800	1.0800	0.8840	-1.5900	22	4.32	63.2
2014-04-04T09:46:42	132.1	32.5	34	0.6020	2.1100	3.9100	1.7600	2.7200	0.7310	22	4.37	74.38
2014-05-29T18:17:59	139.4	33.3	14	-5.2900	3.4200	3.5200	1.5200	-0.5440	-3.0200	22	4.46	72.95
2014-08-29T13:14:35	132.1	32.1	22	2.7700	-1.0100	-0.6080	2.3900	4.5000	-1.8200	24	5.78	82.64
2014-08-29T13:32:03	132.1	32.1	22	3.0400	-0.5990	-0.9730	4.1700	5.2600	-1.7000	22	4.51	45.04
2015-01-02T10:14:06	131.9	32.1	32	0.7340	1.1600	1.9300	0.4440	2.4600	0.1780	22	4.25	79.54
2015-01-31T01:45:54	131.8	31.8	18	4.8100	1.2500	-1.4400	2.9100	3.5800	-0.6980	22	4.45	64
2015-02-06T19:25:10	134.4	33.8	10	0.1400	0.9420	-0.9130	-0.1330	0.2550	-0.4570	23	4.62	85.96
2015-04-19T03:34:54	132.1	32.0	16	0.6220	-0.0366	-0.1890	0.5430	0.7160	-0.1400	23	4.61	70.71
2015-05-20T00:13:18	139.4	34.4	14	1.3100	1.0700	2.6300	-0.0486	0.0517	-4.1800	22	4.38	70.38
2015-05-26T10:35:21	131.9	31.8	22	2.5200	0.0556	-1.5400	1.5700	1.5700	-0.6770	22	4.26	65.76
2015-06-07T01:28:12	139.3	33.0	10	-1.9700	-0.5750	2.1800	0.7020	2.7700	-4.5800	22	4.44	69
2015-07-14T00:52:34	131.8	31.4	28	-1.8300	-0.5050	4.9800	-0.2720	4.7100	1.8100	22	4.47	42.29
2015-07-16T01:18:46	139.2	33.2	12	2.7700	0.3240	4.2400	-2.7500	3.6600	-0.3660	22	4.44	44.73
2015-07-19T11:13:42	131.3	31.3	20	-1.3000	-0.0173	0.6100	-0.8220	-0.9840	0.1300	23	4.74	67.6
2015-07-25T02:53:33	132.4	33.4	40	-4.5800	1.2200	7.4000	0.3360	4.3800	-0.2900	22	4.52	86.6
2015-08-22T01:54:34	132.2	33.3	44	-2.5300	1.6200	4.2100	1.6500	2.2500	1.1500	22	4.38	81.54
2015-08-26T16:51:35	131.9	32.1	34	-1.3000	-0.4380	3.9000	2.4100	1.4700	1.3700	23	5.02	82.74
2015-09-03T01:07:46	134.6	33.3	12	-2.8600	1.7300	1.2900	-0.5470	1.9300	-1.7600	22	4.31	76.71
2015-09-09T05:22:38	138.4	34.7	18	1.2900	-0.4620	0.3680	1.2300	2.2300	4.1400	22	4.40	81.52
2015-12-25T20:20:35	134.5	33.5	32	0.0457	-2.4100	2.6200	-0.6620	0.5150	0.1980	22	4.22	77.08
2016-04-01T20:39:08	136.4	33.4	10	3.7900	-1.4100	-0.6440	5.7600	7.4300	-1.5500	24	5.93	80.84
2016-04-16T16:11:36	131.4	33.3	6	1.5300	4.1900	-1.1700	1.5600	1.1500	-1.4700	23	5.01	83.35
2016-04-16T23:03:55	131.2	33.0	6	0.8010	3.7800	-3.2200	0.3090	1.3600	-1.0300	22	4.33	70.96

2016-04-22T08:20:36	134.3	33.5	30	-0.2900	-3.1100	4.2500	0.4440	0.2300	-0.3540	22	4.32	76.54
2016-04-30T00:09:33	131.4	33.3	6	0.4920	3.7800	-2.2400	1.0300	0.4920	-1.0100	22	4.29	63.2
2016-05-17T02:50:19	131.8	31.8	18	1.7900	0.2350	-0.2700	1.0200	1.3700	-0.3590	23	4.82	73.74
2016-07-12T00:22:00	139.4	33.3	14	-0.5700	1.7900	2.4600	0.6470	0.9710	-1.1000	23	4.89	80.29
2016-07-12T01:58:33	139.4	33.3	14	-2.9800	2.9000	3.2300	1.9700	1.2100	-1.9900	22	4.39	76.06
2016-07-12T02:33:01	139.5	33.2	10	-2.3100	2.5100	2.1900	1.7600	1.0200	-1.7900	22	4.33	58.82
2016-07-12T02:39:39	139.4	33.3	14	-0.5620	2.1100	2.6900	1.2300	0.6250	-1.4000	22	4.26	61.52
2016-07-12T04:31:10	139.4	33.3	14	-1.7100	1.9700	2.7800	1.0100	0.9590	-1.3800	22	4.28	70.48
2016-07-12T14:54:19	139.5	33.3	14	-1.2000	0.3680	0.7810	0.4930	-0.1700	-0.6490	23	4.68	80.11
2016-07-12T15:56:51	139.4	33.3	12	-3.5400	0.9930	3.5400	2.2700	-1.0900	-2.4300	22	4.40	73.1
2016-07-12T16:34:01	139.4	33.3	12	-2.5500	6.2000	5.5900	2.0900	2.5600	-4.3500	22	4.54	75.36
2016-07-13T15:24:51	139.5	33.2	12	-1.1500	2.8200	2.5200	1.0000	0.6950	-1.7300	22	4.30	57.3
2016-07-14T20:05:55	139.4	33.3	14	1.2900	2.5400	2.9600	0.8120	1.1500	-1.1000	22	4.29	20.44
2016-07-14T20:07:06	139.4	33.3	14	-1.0800	3.6400	4.3000	1.5800	1.4800	-2.2600	22	4.41	49.93
2016-07-14T20:17:26	139.4	33.3	12	-2.8500	3.1000	3.0200	1.4000	1.1700	-2.2100	23	5.05	80.29
2016-08-11T01:25:56	131.8	31.8	18	2.0200	0.0648	-0.0248	1.2900	1.9600	-0.4920	22	4.23	69.61
2016-10-22T12:33:44	131.9	32.8	50	3.7400	-4.4500	0.0375	4.7300	3.1400	-0.5440	22	4.50	83.13
2016-11-06T01:57:32	131.9	31.8	18	3.9600	0.6410	-0.3670	1.9800	2.6500	-0.6890	22	4.36	73.58
2016-11-19T20:48:00	135.4	33.9	48	-4.8700	-5.3000	6.4500	2.7200	-0.4450	-5.7800	23	5.25	87.65
2017-02-08T01:21:50	131.5	31.5	18	-1.4600	0.3990	-0.5350	-0.5660	-1.9700	0.0394	22	4.18	56.09
2017-02-08T12:19:26	134.6	33.4	32	0.0980	-2.2400	2.6200	-1.0400	0.3670	-0.7230	22	4.23	77.81
2017-03-03T08:53:42	132.1	32.7	34	-0.4610	2.3400	7.3400	1.5100	4.2700	0.7860	23	5.17	79.75
2017-06-17T07:39:50	131.8	31.9	26	4.4700	0.4820	-1.6800	2.9400	3.2200	-1.3000	22	4.44	80.08
2017-06-21T08:27:39	132.0	32.9	40	0.2360	0.5780	1.3100	1.2700	1.3700	0.6920	23	4.83	81.36

2017-07-02T09:58:21	131.3	33	10	-1.6700	1.9300	-1.3400	0.0344	-1.3000	2.6200	22	4.30	79.73
2017-09-20T03:33:07	132.3	33.4	40	-2.0300	0.9110	2.7200	0.0234	1.3100	-0.8110	22	4.24	78.71
2017-12-05T01:54:11	131.9	32.2	30	0.7080	-0.7160	1.0100	0.7960	1.6400	-0.2400	22	4.15	80.68
2018-01-09T14:51:52	131.8	33.2	40	-0.8680	-4.0500	-0.2880	1.4800	2.8800	-1.4000	22	4.37	29.96
2018-02-19T12:31:36	132.2	32.9	40	-2.4600	-0.1980	3.8100	1.7600	1.4800	-0.2860	23	5.00	84.71
2018-04-23T14:49:36	139.2	34.3	10	4.6400	1.4400	5.3800	0.9050	0.2380	-0.7390	22	4.41	77.28
2018-04-28T22:27:33	131.9	32.0	6	-4.4100	-1.9800	0.1830	-3.7800	-4.5300	0.0852	22	4.49	68.74
2018-06-12T13:54:20	131.5	31.1	30	2.0100	0.1340	-0.5320	0.6840	1.1400	-0.5430	24	5.48	74.03
2018-10-05T02:20:52	131.2	31.0	30	8.6400	-0.6640	0.1650	2.2500	4.7300	-2.2400	22	4.55	68.18
2018-11-03T01:53:53	135.2	33.7	40	-0.4100	0.0548	0.4150	0.2260	-0.6330	-0.8110	24	5.30	89.27
2018-11-05T17:19:13	135.3	33.7	46	-0.9130	-4.3300	4.4300	2.1900	-1.7500	-4.0400	22	4.48	81.7
2019-01-22T08:17:07	132.4	32.9	28	0.0827	-1.7100	1.7500	-0.2720	0.2710	0.3020	22	4.10	74.62
2019-03-12T00:37:48	132.7	33.2	34	-0.3650	-0.8620	1.0900	0.3180	0.2010	-0.5390	23	4.66	79.17
2019-03-13T22:48:46	134.9	33.8	38	0.2280	-6.3100	5.0700	-0.8290	-1.8600	-1.6400	23	5.13	84.24
2019-03-27T18:11:22	132.1	32.1	22	3.7800	-1.4500	-1.7600	3.2600	6.4300	-2.7900	23	5.21	83.68
2019-03-28T00:38:03	132.1	32.2	22	4.5800	-0.4790	-1.9300	4.6800	7.6100	-2.3900	23	5.26	84.47
2019-04-23T16:49:49	131.2	31.3	24	-1.8200	0.0989	0.5650	-1.2600	-2.2800	-0.0562	22	4.24	73.07
2019-05-10T16:43:23	131.9	31.8	20	3.2900	0.2030	-0.9640	2.1500	2.7900	-0.7340	24	5.69	73.07
2019-05-10T17:48:45	131.8	31.9	26	1.4000	0.1140	-0.5820	1.1400	1.5300	-0.4370	25	6.17	80.1
2019-05-10T18:07:36	131.9	31.8	26	2.5400	0.4640	-1.4000	0.9410	0.9770	-0.1030	23	4.86	50.82
2019-05-10T22:53:52	131.9	31.8	22	2.7100	1.2700	-1.6300	2.0200	1.1000	-0.8500	22	4.29	47.78
2019-05-11T05:40:37	131.8	31.8	28	4.2100	-2.7500	-2.5600	2.6500	5.0600	-2.0400	22	4.51	77.56
2019-05-11T17:59:38	132.3	32.7	32	-0.2330	0.2990	1.4400	0.3300	1.3200	-0.1170	23	4.76	87.79
2019-05-13T00:07:41	132.3	32.7	32	-0.9350	0.6150	2.5100	0.2610	1.9400	-0.0225	22	4.23	77.08

2019-06-19T20:35:44	131.2	31	32	3.8600	-0.1390	0.3560	1.2000	2.9300	-0.7980	22	4.35	58.62
2019-07-27T11:11:46	131.8	31.6	24	2.7700	-0.5160	0.8590	1.4300	2.5800	-1.4700	22	4.33	80.01
2004-04-21T07:26:30	132.3	33.5	38	-1.5100	-1.8500	2.9000	-2.4800	-1.2300	1.3700	22	4.34	67.45

Table S2. CMT solutions for the M_w 7.2 and 7.5 earthquakes.

Centroid time (UTC)	Lon.	Lat.	Depth [km]	M_{rr}	$M_{\theta\theta}$	$M_{\phi\phi}$	$M_{r\theta}$	$M_{r\phi}$	$M_{\theta\phi}$	Exp.	Mw	VR [%]
2004-09-05T 10:07:12	136.7	33.1	26	0.4435	-7.6109	-2.2143	-0.331	0.4022	0.3545	26	7.10	71.76
2004-09-05T 14:57:43	137.0	33.2	20	0.6117	-1.3773	-0.0418	-0.3787	0.1300	0.1093	27	7.31	71.83